Computational Study of the Lift to Drag Ratio of Lifting Body Aircraft with Volumetrically Equivalent Fuselages of Different Profiles

by

Md Mahbubul Islam

Submitted in partial fulfillment of the requirements for the degree of

MASTER OF SCIENCE IN MECHANICAL ENGINEERING

Department of Mechanical Engineering

BANGLADESH UNIVERSITY OF ENGINEERING AND TECHNOLOGY

Dhaka 1000, Bangladesh.

June, 2011

This thesis titled "**Computational Study of the Lift to Drag Ratio of Lifting Body Aircraft with Volumetrically Equivalent Fuselages of Different Profiles",** submitted by **Md Mahbubul Islam**, Student No. **0409102048P** Session April 2009 has been accepted as satisfactory in partial fulfillment of the requirement for the degree of MASTER OF SCIENCE IN MECHANICAL ENGINEERING on June 25th , 2011.

BOARD OF EXAMINERS

1._____ Chairman

Dr. Mohammad Mamun
Associate Professor,
Department of Mechanical Engineering
Bangladesh University of Engineering and Technology
Dhaka-1000, Bangladesh.

2._____ Member
(Ex-Officio)

Dr. Muhammad Mahbubul Alam
Professor and Head,
Department of Mechanical Engineering
Bangladesh University of Engineering and Technology
Dhaka-1000, Bangladesh.

3._____ Member

Dr. Md Quamrul Islam
Professor,
Department of Mechanical Engineering
Bangladesh University of Engineering and Technology
Dhaka-1000, Bangladesh.

4._____ Member

Dr. Mohammad Ali
Professor,
Department of Mechanical Engineering
Bangladesh University of Engineering and Technology
Dhaka-1000, Bangladesh.

5._____ Member
(External)

Dr. Md Shafiqul Islam
Director, Central Engg. Facilities
Atomic Energy Research Establishment, Savar,
Dhaka, Bangladesh

CANDIDATE'S DECLARATION

It is hereby declared that this thesis or any part of it has not been submitted elsewhere for the award of any degree or diploma.

Signature of the Candidate

_____

Md Mahbubul Islam

Dedicated to my parents

TABLE OF CONTENTS

LIST OF FIGURE

LIST OF TABLE

NOMENCLATURE

Notation	Definition
ρ	Density of the fluid
μ	Dynamic viscosity of the fluid
υ	Kinematic viscosity of the fluid
C_L	Lift Coefficient
C_D	Drag Coefficient
L	Lift force
D	Drag force
θ_f	Fuselage angle of attack in degree
θ_w	Relative angle between wing and fuselage
u, v, w	Velocity components in x, y and z direction respectively
U_p	Velocity of the particle
p	Pressure of the flowing fluid at any point within the channel
f_b	Fluid body force
τ_{ij}	Viscous stress tensor
σ_{ij}	Total stress tensor
Re	Reynolds number
c	Chord length
L/D	Lift to drag ratio

ACKNOWLEDGEMENTS

At first I would like to express my gratitude to Almighty Allah for giving me the opportunity of performing this work. I also want to thank my parents and my elder brother for giving me unquestionable support to continue my graduate study.

I want to express my gratefulness to my supervisor Dr. Mohammad Mamun who has guided me through the course of my graduate study and research. Without his guidance, support and suggestion this thesis was nearly unthinkable to complete. He has drawn my attention to various aspects of fluid mechanics and motivated me for the fundamental research work. I also give heartiest thanks to Dr. Md. Quamrul Islam, Dr. Muhammad Mahbubul Alam, Dr. Mohammad Ali and Dr. Md Shafiqul Islam for their valuable suggestions.

I am very grateful to Mr. Ashim Ali,whose assistance and expertise on grid generation in the finite volume software helped me greatly. I want to extend my personal gratification to Trieu Nguyen from Vietnem and Robin Gaupp from Germany who have given me very helpful and informative suggestions throughout my thesis.

I would also thanks to Mr. Faruk Ahmed Sohag and my friend Mr. Rajib Kumar Saha for their valuable advices and inspiration. I also acknowledge the heartiest gratitude to my other colleagues for their kind encouragement.

ABSTRACT

In this thesis, the effect of airfoiled fuselages on the improvement of overall lift to drag ratio of Unmanned Aerial Vehicle (UAV) is investigated, where along with the wing, fuselage also provides some lift. To compare the lift to drag ratio, two different types of fuselages are considered, one is conventional circular and another is airfoil cross-section. A three dimensional finite volume model is developed for numerical investigation of volumetrically equivalent fuselages. Spalart-Allamaras model is chosen as turbulence model. Hexahedral volume meshing is used with suitable boundary conditions. Developed finite volume model is validated with the available experimental data and farther investigation is carried out for different wing angle and angles of attack. Although at lower angle of attack lift coefficients for airfoiled fuselages are substantially higher as well as high drag coefficients which results lower lift to drag ratio but at higher angle of attack remarkable improvement of lift to drag ratio is noticeable. From the results, the optimum angle of attack at different speeds during takeoff, cruise and landing of the low speed UAVs are also found.

CHAPTER 1
INTRODUCTION

1.1 Background and Motivation

The major thrust in designing of an aircraft is to increase its lift along with the reduction of drag. From the early 20^{th} century research works have continuously been carrying out on these facts at different forms to develop the most efficient airfoil section which would produce the maximum lift corresponding to relatively small drag. For different airfoil profiles, coefficient of lift ($C_{L)}$ and that of drag ($C_{D)}$ have been measured or calculated. The airfoil section used in conventional airplane wings which basically produce the lift while its fuselage has little or no contribution in it. But the appreciable portion of total drags is contributed by the fuselage. The total drag produced by each exposed parts of the airplane should be minimum such that overall lift to drag ratio is maximum. So the designing of an airplane should also include the reduction of drags of all its exposed parts. On the other hand if it is possible to extract some lift from each exposed parts then that would also maximize the overall lift to drag.

So in order to maximize the efficiency of an aircraft, the basic design premises should be such that all elements/components of the aircraft must contribute to the aircraft lift. In pursuit of this goal and to solve the present challenges and future goals of the air transportation system of increased efficiency, passenger safety and productivity combined with greater personal mobility and expanded transportation capability, the scientific community is now turning their attention to the lifting-body aircraft. The lifting-body aircraft design principle allows the designer both safe and fuel-efficient aircraft for an efficient utilization of the air transportation system for the movement of people and goods. This design would also provide increased payload and a dramatically improved short take-off and landing (STOL) capability, over conventionally designed [1-5] aircraft. In conventional design the aircraft, fuselages are generally circular and the wings are airfoiled shaped. Although the circular fuselage has less drag but it produces no lift. Instead of circular fuselage if an airfoiled section fuselage is incorporated in an airplane then it will produce some lift and will be expected to increase overall lift to drag ratio. The airplane with airfoiled section fuselage is termed as lifting body aircraft.

1.2 Objectives of the Thesis

The specific objectives of the present research work are as follows:

(a) To establish a computational model to investigate the lift and drag coefficients of fuselages.

(b) Established model will be validated with the data obtained from the experiments.

(c) With the established computational model, the characteristics of the overall lift to drag ratio of volumetrically equivalent fuselages of different profiles in the speed range of 50-100 km/hr at different angle of attacks will be investigated.

1.3 Overview of the Present Work

In this research, in addition to the conventional circular cross-section fuselage, airfoil fuselage is introduced which produces some lift from the fuselages and increase the total lift force generated. Both types of fuselages are used for finite volume simulation to calculate the lift and drag coefficients using suitable boundary conditions and turbulence models for different angle of attacks and to find out the best fuselage corresponding to overall lift to drag ratio. Numerical results are then validated using the available experimental data for these models. By comparing the results it is also found out what should be the best angle of attack of the fuselage at different speeds during takeoff, flying and landing condition.

1.4 Outline of the Thesis

A detail literature review is provided in Chapter 2. The wing design methodology in CAD software, surface and volume meshing of the model is described in Chapter 3. Geometry generation of the model in the CAD software to be suitable for Computational Fluid Dynamics (CFD) simulation, different meshing schemes, meshing procedures and selection of boundary conditions are also described. Numerical procedure, choice of suitable turbulence model is delineated in Chapter 4. Along with these a flowchart of the overall solution methodology is also provided. Chapter 5 presents the simulation results. First the model is validated by comparing the calculated lift and drag coefficients of a lifting body aircraft of airfoil cross sectioned fuselage with the available experimental

data. In the later sections, the values of the L/D ratios of other models were calculated within operating range. In Chapter 6, the conclusion and the recommendations for future works are presented.

CHAPTER 2
LITERATURE REVIEW

In early 20th century a famous professional aircraft designer Vincent Justus Burnelli [6] developed the concept of lifting body aircraft where he used fuselages of airfoil cross section. But this fuselage airfoil section had to be sufficiently thick such that man could ride on it. So the scientific community had raised a number of technical concerns related to the large fuselage and its impact on aerodynamics. Amongst these primary concerns was the negative aerodynamic drag effects attributed to the lifting-body fuselage due the increased fuselage frontal area and the fuselage wing interference. Fig. 2.1 shows the Burnelli's designed first airfoiled section fuselage bi-plane [6]. The bi-plane was very large, capable of carrying 26 passengers.

Fig. 2. 1 Bernelli's lifting body fuselage bi-plane, RB-1

An analysis of the concept performed by Wertenson [7, 8] in 1931 showed that the Burnelli's design concept resulted in less frontal area than a conventional twin-engine transport airplane and that the negative fuselage wing interference is more than compensated by the increased lift of the fuselage. Subsequent analysis performed at that time by some researchers [9-12] also supported the findings of Wertenson.

The primary focus of Burnelli's research at Lawson Airplane Company of Green Bay and Milwaukee, WI at the end of the First World War was aimed at to build airplanes for peace instead of war. As his research outcome Burnelli built American's first twin engine airplane. This basic element of the Burnelli design principle is just now being

considered and utilized by the aeronautical community for a variety of vehicle classes that vary from personal air vehicles (PAVs) to jumbo transports. It is important to note that Burnelli was not alone in the development of all-lifting vehicle technology, there were more than fifty all-lifting aircraft developed during the last century [6, 13]. But all of these aircraft were designed for large carrying capacity. But now-a-days small Unmanned Aerial Vehicle (UAV) concepts are developed and this UAV does not require thicker fuselage besides it uses sophisticated electronic elements that are small in size but heavy. So UAV requires higher lifting force with a smaller size. National Aeronautics Space Administration's (NASA) X-39, X-43B, X-45A and all Unmanned Combat Aerial vehicle (UCAV) also uses all-lifting body fuselage but all of these are designed for high-speed transport under Future Aircraft Technology Enhancements (FATE) program [14,15].

As some of the UAV for area reconnaissance or similar purposes have to operate in the speed of 50km/hr to 100km/hr, the present investigation is carried out in this speed range. On the other hand, we should follow the design of nature and the practical aspects of streamline form may be studied from the bodies of fishes and birds, the profiles of which have gradually met the requirements of least resistance for motion through a fluid, water or air, as the case may be [16]. In this context the gliding bird's body shape could be a good natural example for a UAV design and for most of the gliding birds like Harris' hawk (*Parabuteo unicinctus*) have airfoil body shape rather than conventional cylindrical shape [17]. Fig. 2.2 shows the body shape of a Harris' hawk during flying condition.

Fig. 2. 2 Lifting body shape of a Harris' hawk (*Parabuteo unicinctus*)

Again during their flights, birds continuously change their feathers position to improve their maneuvering capability with minimum energy loss. For example the feathers at the wing tips of most birds that soar over land separate both horizontally and vertically in flight to form slotted tips as shown in Fig 2.3. The individual feathers in the slotted tips resemble the winglets used on the wing tips of some aircraft to reduce induced drag.

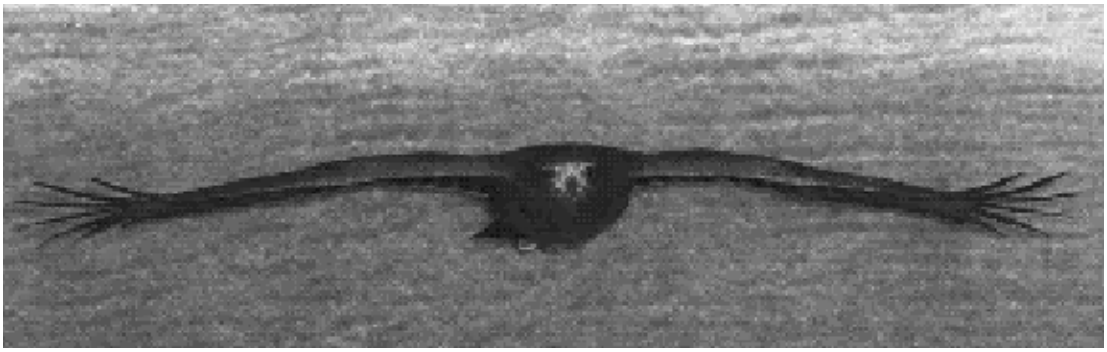

Fig. 2. 3 The Harris' hawk (Parabuteo unicinctus) is gliding with vertical separation between the feathers in the slotted wing tips.

V. A. Tuckerm [17] made an extensive research on the lift drag characteristics on wings creating the similar conditions of birds' wings. He found that a wing that produces lift leaves a pair of vortex sheets in its wake which generates the induced drags. The feathers at the wing tips of most birds that soar over land separate both horizontally and vertically in flight to form slotted tips i.e. the winglets and the wing theory shows that winglets can reduce the kinetic energy left in the vortex sheets, and hence the induced drag, by spreading vorticity both horizontally and vertically. He also found that the total drag of the wing with the feathered tip was 12% less than that of a hypothetical wing with the same lift and span, but with tip feathers that did not respond to upwash at the end of the base wing. This value is consistent with wing theory predictions on drag reduction from winglets and the Wings with the tip and the base wing locked together had lift and drag that increased with increasing base wing angle of attack, as expected for conventional wings without winglets. [18- 24].

Eastman N. Jacobs and Albert Sherman [25] tests of wing-fuselage combinations employing an airfoil-type fuselage were made in the variable-density wind tunnel as a part of the wing-fuselage interference program and the test results showed that the airfoil-type-fuselage combination should be well faired in such a way as to eliminate the

discontinuity at the ends of the fuselage. The results show that the fuselage part of the lifting surface, comprising 33 percent of the total lifting area (exposed wing area plus fuselage area) contributes 26 percent of the total lift.

I. Kroo [26] from Stanford University recently performed some research works aiming to increase the commercial aircraft efficiency. His findings shows that the vortex drag of commercial aircraft accounts for a large fraction of airplane cruise drag (typically about 40%) and therefore concepts that result in reduction of vortex drag may have a significant effect on fuel consumption. Vortex drag is even more significant at low speeds where vortex drag typically accounts for 80%-90% of the aircraft's climb drag at critical take-off conditions [26]. Although take-off constitutes a very small portion of the flight, but its influence on the overall aircraft design is profound. Since conditions associated with engine-out climb shortly after take-off are often critical constraints in the aircraft design, changes in aircraft performance at these conditions influence the overall design and so have an indirect, but powerful, effect on the aircraft cruise performance. While a 1% reduction in drag due to lift might improve the cruise lift-to-drag ratio by 0.4% with a similar effect on range, the improved low speed climb performance may make it possible to achieve acceptable take-off and climb with almost 1% greater take-off weight, leading to an increase in range several times that associated with the simple cruise L/D improvement [26, 27]. Furthermore, lower drag at high lift conditions leads to reduced noise. He also noted that the induced drag may be easily reduced by increasing the span of a planar wing. A 10% increase in wing span leads to a 17% reduction in vortex drag at fixed speed and lift [26]. But the primary reason that wing spans are not increased to reduce drag is that the higher structural weight and cost make such efforts counterproductive. To produce a large change in the vortex drag without a large increase in wetted area, his low aspect ratio endplates were replaced with higher aspect ratio winglets.

In a recent study, an experimental investigation was performed by M. Mainuddin [28], to improve the overall lift to drag ratio of an UAV by reducing the induced drag with the employment of winglets with an airfoil cross-section fuselage.

Formulas for Lift and Drag Coefficient Calculation

The equation for Lift Coefficient is**:**

$$C_L = \frac{L}{\frac{1}{2}\rho V^2 S_{ref}} \tag{2.1}$$

The equation for Drag Coefficient is:

$$C_D = \frac{D}{\frac{1}{2}\rho V^2 S_{ref}} \tag{2.2}$$

Where ρ is the density of air, V is the relative velocity between the wing and air, L is lift force, D is the drag force and S_{ref} is reference area. For lift coefficient it is the area of the wing when viewed from overhead i.e. the chord length times the wing span, in case of drag coefficient reference area is the projected frontal area.

CHAPTER 3
DESIGN METHODOLOGY

A number of volumetrically equivalent fuselage models with airfoil and conventional circular cross section are used in this investigation. Geometrical features and construction methodology will be described in this chapter.

3.1 Wing and Fuselage Profiles

NACA four digit series airfoil sections are suitable for low speed aircraft so it is considered for wings in this investigation. Same set of wings are used in both the cylindrical and airfoiled fuselage models so that the results can be shown for the comparison between the fuselages. NACA four digit series are considered for the airfoiled fuselages as well.

3.1.1 NACA Four-Digit Series Airfoil

The first family of airfoils designed using this approach became known as the NACA Four-Digit Series. The first digit specifies the maximum camber (m) in percentage of the chord (airfoil length), the second indicates the position of the maximum camber (p) in tenths of chord, and the last two numbers provide the maximum thickness (t) of the airfoil in percentage of chord. For example, the NACA 2412 thickness of 12% with a camber of 2% located 40% back from the airfoil leading edge (or 0.4c).

Fig. 3.1 shows the cross-section of an NACA 2412 cambered airfoil wing section.

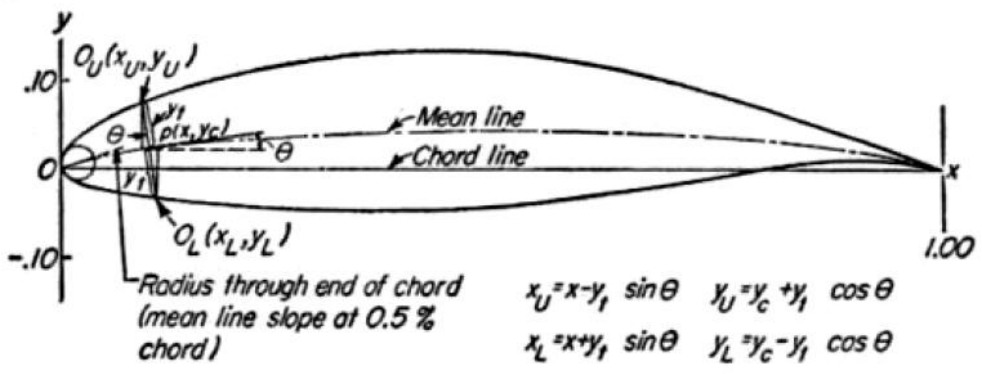

Fig.3.1 NACA Airfoil geometrical construction

The mean camber line coordinates by plugging the values of m and p into the following equations for each of the x coordinates.

$$y_c = \frac{m}{p^2}(2px - x^2) \qquad \text{from x = 0 to x= p} \qquad (3.1)$$

$$y_c = \frac{m}{(1-p)^2}[(1-2p) + 2px - x^2] \qquad \text{from x = p to x = c} \qquad (3.2)$$

where

x = coordinates along the length of the airfoil, from 0 to c (which stands for chord, or length)

y = coordinates above and below the line extending along the length of the airfoil, these are either y_t for thickness coordinates or y_c for camber coordinates

t = maximum airfoil thickness in tenths of chord

m = maximum camber in tenths of the chord

p =position of the maximum camber along the chord in tenths of chord

The thickness distribution above (+) and below (-) the mean line is calculated by plugging the value of t into the following equation for each of the x coordinates.

$$\pm y_t = \frac{t}{0.2}\left(0.2969\sqrt{x} - 0.1260x - 0.351x^2 + 0.2843x^3 - 0.1015x^4\right) \qquad (3.3)$$

The final coordinates for the airfoil upper surface (x_u, y_u) and lower surface (x_l, y_l) using the following relationships.

$$x_u = x - y_t \sin\theta \qquad (3.4)$$

$$y_u = y_c + y_t \cos\theta \qquad (3.5)$$

$$x_L = x + y_t \sin\theta \qquad (3.6)$$

$$y_L = y_c - y_t \cos\theta \qquad (3.7)$$

Where $\theta = \arctan\left(\frac{dy_c}{dx}\right)$

The vertex data are calculated using a C-program.

3.2 Three-dimensional model

Modeling started with the generation of a Computer Aided Design (CAD) model. The vertex data are calculated using a C-program. Then the geometry for the models used in simulation is created on Rhinoceros subsequently used for the Computational Fluid

Dynamics (CFD) simulation. The size of all models remains unchanged with 1:1 full scale. A rectangular shape boundary region is generated around the wing model. Sufficient spacing between aircraft model and boundary region is provided for appropriate meshing and simulation. Since the models have mirror symmetry relative to x-y plane, it is possible to split the model in half in order to create a finer mesh, and which saves memory during simulation.

The NACA 2412 cambered airfoil wings with a chord 80 mm and a total span of 200 mm are used for both the models. Fig. 3.2 shows the cross-section of an NACA 2412 cambered airfoil wing section.

Fig. 3.2 The real size cross-section of the model wings

Chord length and span of the fuselage cross-section model are 238 mm and 100 mm respectively. Circular section model has a total length of 274 mm with 44 mm long nose section, 70 mm long tail section and 160 mm long circular body with a diameter of 50 mm. The detail section is shown below in Fig. 3.3. Volume of both the model is 438400 mm^3 as found in Rhinoceros.

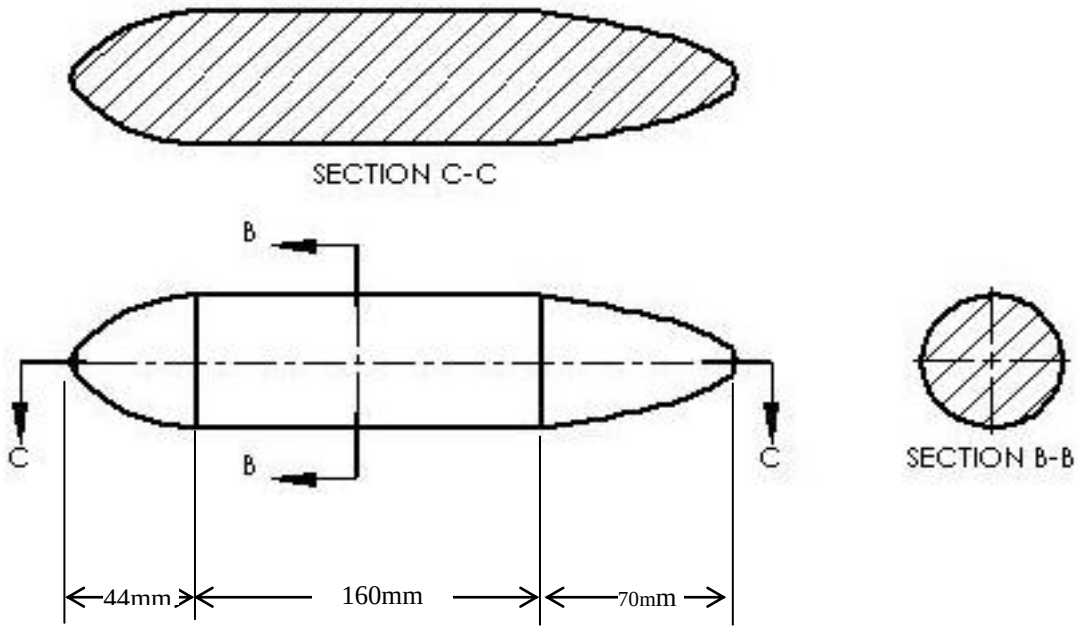

Fig. 3.3 Cross section of the circular fuselage

The geometries designed in CAD software are shown in Fig. 3.4. In Fig. 3.5 the model is spilled in half for symmetric analysis.

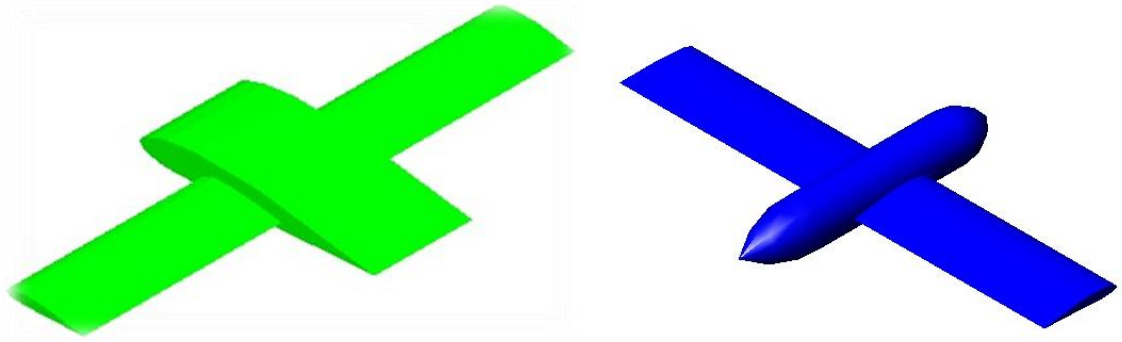

(a) Airfoiled fuselage (b) Cylindrical Fuselage

Fig. 3.4 Volumetrically equivalent CAD Model of aircrafts

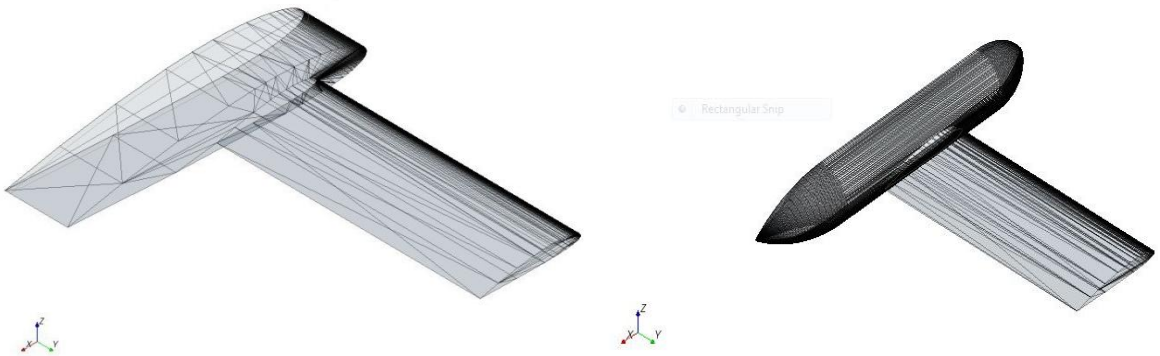

(a) Airfoiled fuselage (b) Cylindrical Fuselage

Fig. 3.5 Symmetric model of volumetrically equivalent aircraft

After importing the IGES format of the geometry at the finite volume software, the boundaries of the domain is splitted to assign different boundary conditions.

The boundary conditions which are set for the boundaries are as in the Table 3.1.

Table 3.1 The boundary conditions

Name	**Type**
Inlet	Velocity inlet
Outlet	Pressure Outlet
Wing+ Fuselage	No-Slip Wall
Top, Bottom and Side wall	Slip Wall
Symmetry Plane	Symmetry

As it's not necessary to simulate the boundary layer of the top, bottom and the side wall, therefore, these three walls are set as slip-wall. And only the fuselage surface is no-slip wall. At the slip wall no boundary layer will be developed so, no need to refine the meshes near the slip-wall, thus computation is reduced.

3.3 Surface and Volume meshing

Meshing is a vital step for CFD simulation. Mesh is defined as geometry and space on model being solved by mathematical methods of fluid dynamics. Volume mesh is composed of three basic mesh elements; vertices, faces, and cells. Individual cells are connected and formed within boundary region of the model to be computed in the simulation. Therefore, refinement of the meshes has major effects on accuracy of the simulation results. It may be true that greater numbers of mesh cells yield better chances of obtaining more accurate results; nevertheless, other factors must be considered, such as time and computer capability. Quality and validity of mesh are also as important because it concerns to validity of results being computed at certain space.

The software used for the simulation is equipped with a powerful meshing capability. The semi-automatic meshing tool allows user ease of generating both surface mesh and

volume mesh. The tool allows a user to focus solely on interacting with region and boundary of model, rather than mesh elements.

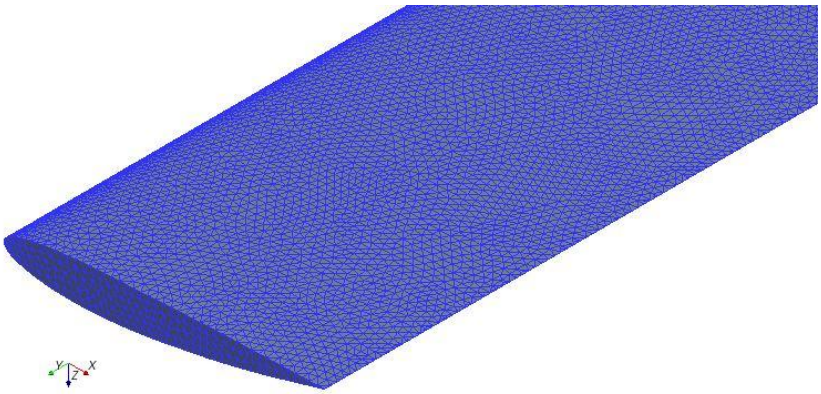

Fig. 3.6 Surface mesh at wing

Surface mesh serves as starting for volume meshing. Surface originated by CAD software; generally is not of good quality, unless created and exported into mesh files. In this case, surface is created by CAD software, and is imported as IGES format into the finite volume software. These meshes are not constructed, and its quality is too poor for volume meshing. The software offers options to regenerate, improve triangulation, and prepare surface mesh in order to obtain a high quality volume mesh. Such features used in this simulation case are surface remesher, and surface wrapper. Surface wrapper includes features to literally wrap surface in order to create or ensure a watertight model. This is an ideal function for repairing imported poor quality surfaces with intersecting surfaces, holes, and gaps, which is not for initiation of volume meshing. Surface remesher offers re-triangulation features to produce higher quality surface. It also enhances surface triangulation resolution. It is typically used in cooperation with surface wrapper to improve poor quality closed surfaces.

The volume mesher contains three different types of volume mesh, each of which offers advantages and disadvantages of their own kinds. There three types are tetrahedral, polyhedral, and trimmer mesh. The tetrahedral volume mesher offers tetrahedral shape based core mesh. It provides an efficient and simple solution, which in turn uses the least amount of time and memory for a given number of cells. This, however, requires five to eight times more mesh density than polyhedral and trimmer mesh to obtain the same accuracy. It could be an ideal method when not much accuracy is required. Polyhedral mesher produces arbitrary polyhedral shape based core mesh. It provides a solution for

complex mesh generation problems. Polyhedral mesher is relatively easy and efficient to execute. Polyhedral mesh contains approximately five times fewer cells than tetrahedral mesh for a given starting surface, and is more efficient. Both tetrahedral and polyhedral mesher is dependent on the quality of the surface mesh, meaning that bad quality surface mesh will lead to poor quality volume mesh.

Trimmer mesh produces trimmed mesh based on hexahedral shaped core mesh. It is similar to structured mesh, and provides high quality grids. Its methodology is robust and efficient for both simple and complex mesh generation problems. It utilizes hexahedral template mesh in which it is trimmed based on starting input surface. Unlike tetrahedral and polyhedral, trimmed mesher is independent on quality of starting surface. This means that bad quality of surface will not lead to bad quality of volume mesh, and implies that it likely will produce good quality volume mesh in most circumstances. For reason above, trimmer model is chosen to be a volume mesher used in the simulations, because it provides efficiency, quality and robustness of generated mesh. The comparison of three types of volume meshing is shown in Fig. 3.7.

Fig.3.7 Three types of volume meshing; left: tetrahedral, middle: polyhedral, right: trimmer.

The quality of mesh depends on another factor which is grid density. It is very important for the volume mesh to contain a sufficient amount of grids at all or specific regions on the model. In certain regions where there are rapid changes in aerodynamic properties, a finer mesh is required in order to follow greater details of study of those changes, and enhance the accuracy of the results. Sometimes, these changes or aerodynamics properties occur due to shape complexity. It is beneficial to refine the number of mesh

cells as this helps in maintaining the true shape of the model. In other region where finer mesh is not necessary, it is still important to assign a sufficient amount of grid cells because it may affect overall results.

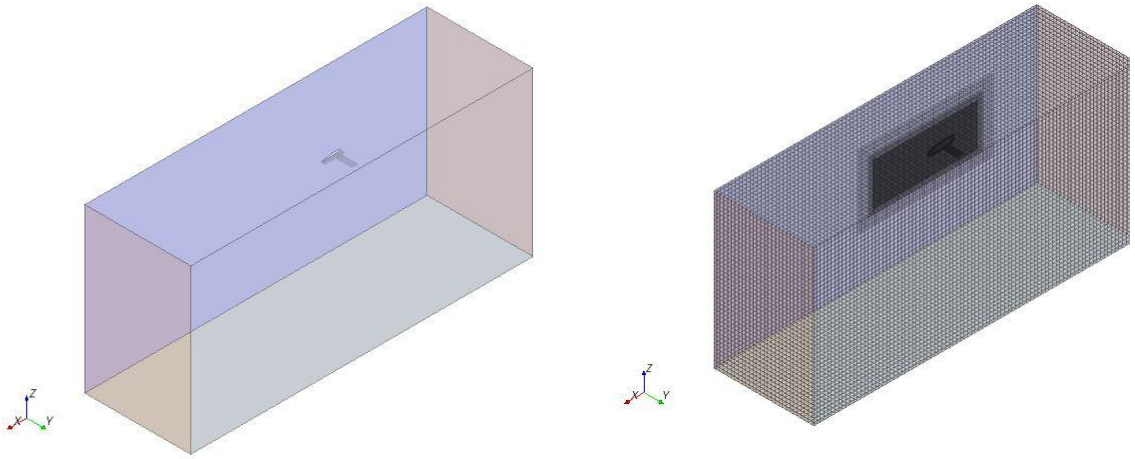

(a) Before mesh (b) After mesh

Fig. 3.8 Flow domain

Fig. 3.8 shows fluid domain before and after mesh. The mesh in the far field no needs to refine while near the model surface, the volume control is used with smaller cell size to refine the mesh in this region. It's necessary for solving the flow near the wing surface.

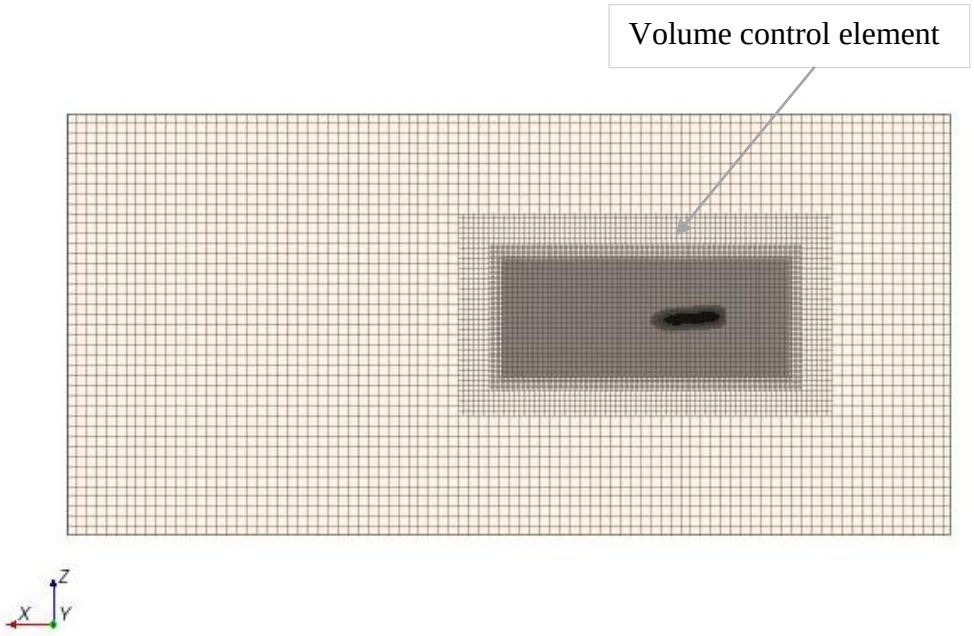

Fig. 3.9 Volume control element around the fuselage

There is another useful tool, called volume shape, to adjust grid density where needed. Volume shape can be used prior to generation of volume mesh. Three shapes could be assigned on the model, brick, cylinder, and cone. Regions where these volume shapes are placed on can be assigned different grid densities. This tool is very efficient for assigning specific grid density where needed. Volume control element used in this model shown if Fig. 3.11. Thus, the first region that needs to be considered for finer mesh is near the wing itself. Secondly, another vital region is the wake. It is necessary that a sufficiently fine mesh needs be applied to maintain wing shape and characteristics, because the wing is a primary source of aerodynamic forces. There should be sufficient amount of fine grids in front of the model such that alteration of forces can be thoroughly and properly calculated.

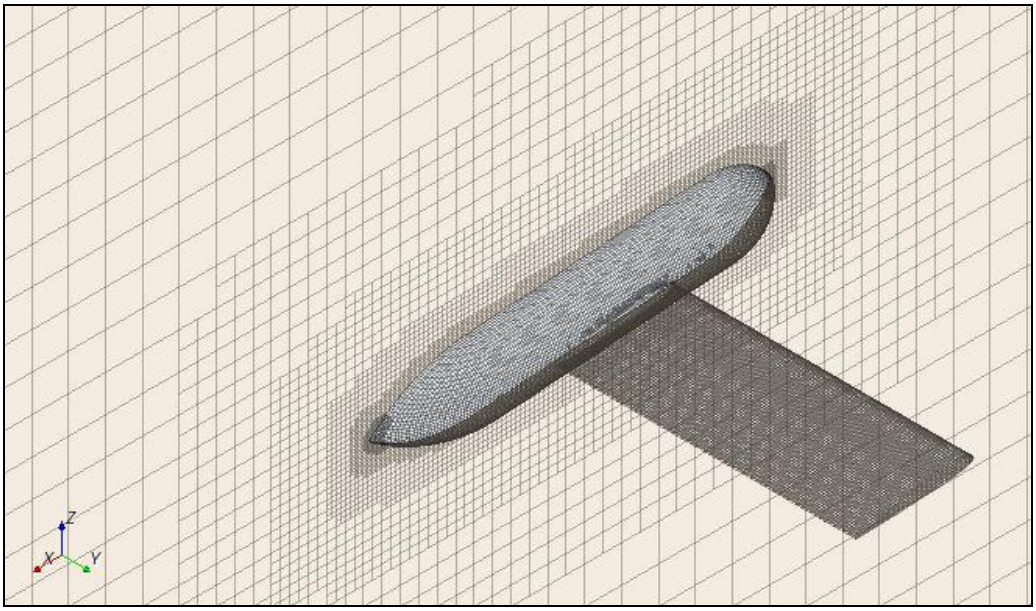

Fig. 3.10 Volume mesh near circular fuselage

Volume meshes near the airfoil fuselages are shown in Fig. 3.10 and around the circular fuselages are shown in Fig. 3.11. During meshing first cell height is set based on the Y-plus value. Y-plus values used in this investigation are near 50 which correspond to coarse meshes. This wall function parameter has a very important role on the solution. Generally for finer mesh Y+ value is chosen less than 5 and for coarse meshes greater than 30.

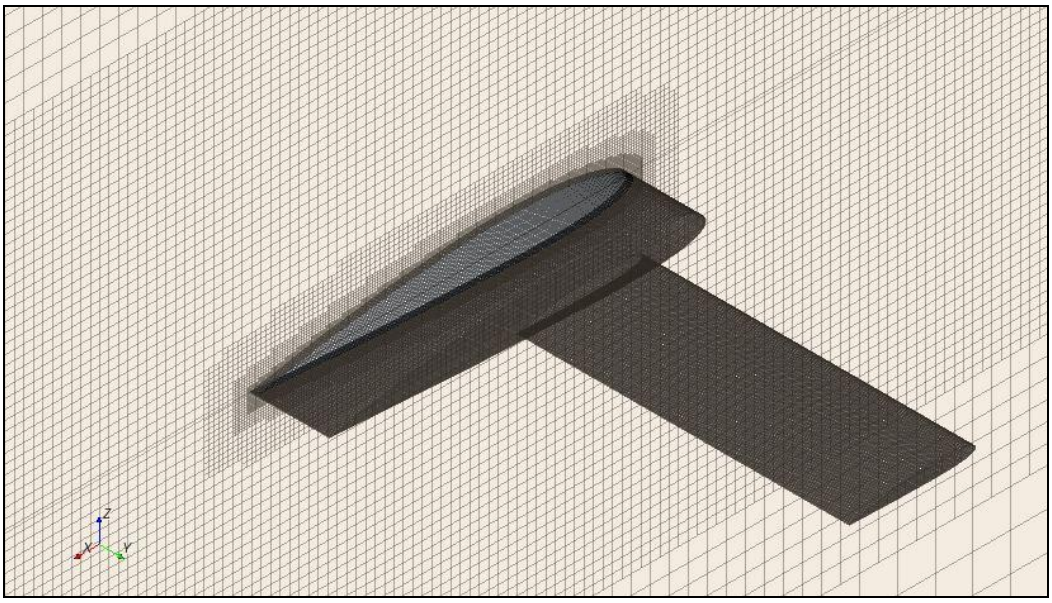

Fig.3.71 Volume mesh near airfoil fuselage

The wing and fuselage surface mesh with the surface size is set equal to one tenth of the base size in order to generate a very fine mesh as shown in Fig. 3.6. The prism layer mesh is used to create a very fine mesh near the wing and fuselage surface as in Fig. 3.12.

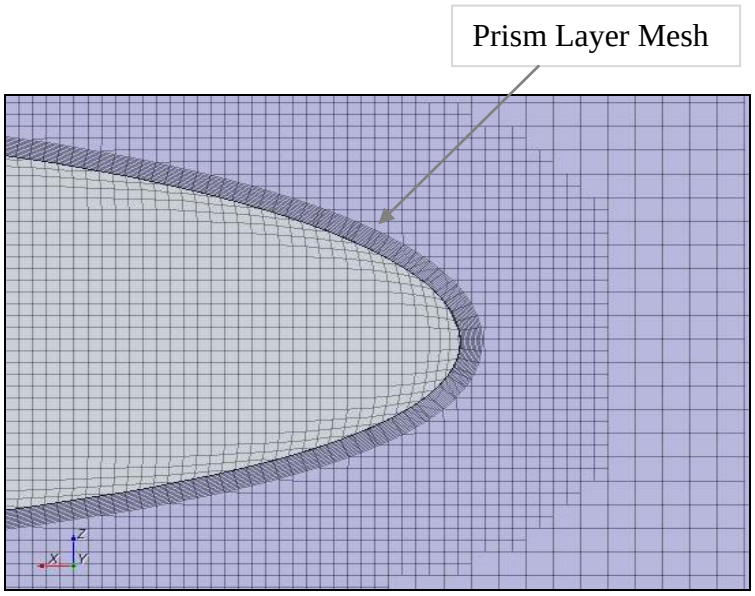

Fig.3.8 The finer volume mesh near the leading edge

In order to capture the wake generated at the trailing edge of the fuselage Trimmer wake refinement feature also used in mesh generation to refine meshes to capture the wake generated at the trailing edge.

CHAPTER 4
NUMERICAL SOLUTION METHODOLOGY AND SIMULATION

4.1 Finite Volume Method

The finite volume method is a discretization method which is well suited for the numerical simulation of conservation laws; it has been extensively used in fluid dynamics fields. The finite volume software STAR CCM++ 4.04 is used for the simulation. The governing equations associated with this thesis will be described in the next sections.

4.1.1 Navier-Stokes equation

The Navier-Stokes (momentum) equation for incompressible flow can be expressed as

$$\frac{\delta u_i}{\delta x_j} = -\frac{1}{\rho}\frac{\delta p}{\delta x_i} + \frac{\delta}{\delta x_j}\left[v \left(\frac{\delta U_i}{\delta x_j} + \frac{\delta U_j}{\delta x_i}\right)\right] + f_i \qquad (4.1)$$

Here u_i denotes the velocity component in the direction of the Cartesian coordinate xi; p is the pressure; ρ is the density; υ is kinematic viscosity, and t is the time. The body force f_i is dropped in the further discussion because it can be combined with p if only the gravity force is involved.

The scalar continuity equation, which accounts for mass conservation, is:

$$\frac{\delta u_i}{\delta x_i} = 0 \qquad (4.2)$$

Generally these equations cannot be solved analytically because of the nonlinearity of the Navier-Stokes equations and, even more, because of the non-analytical and, may be due to complex body shape. Therefore, a numerical method is applied to solve them.

4.1.2 Reynolds Averaged Navier-Stokes Equation

Although Navier-Stokes equations are generally considered to govern both laminar and turbulent flows, practically they are not directly suitable for computing turbulent flows. One of the reasons is- in turbulent flows because of the fluctuations, velocity and pressure is a rapidly varying random function of time and space. Thus, physical

quantities like velocity, stress etc. should be averaged over time. The velocity u_i and pressure p can be divided into the mean part U_i, P and the fluctuating parts $\acute{u}_i$, $\acute{p}$:

$$u_i = U_i + \acute{u}_i \quad p = P + \acute{p} \tag{4.3}$$

If (4.3) is substituted into (4.1) and the time averaging procedure is then applied to (4.1), the steady Reynolds-Average Navier-Stokes equations (RANSE) are obtained as

$$\frac{\delta(U_i U_j)}{\delta x_j} = \frac{1}{\rho}\frac{\delta P}{\delta x_i} + \frac{\delta}{\delta x_j}\left[\nu\left(\frac{\delta U_i}{\delta x_j} + \frac{\delta U_j}{\delta x_i}\right)\right] - \frac{\delta(\overline{\acute{u}_i \acute{u}_j})}{\delta x_i} \tag{4.4}$$

Where $\overline{\acute{u}_i \acute{u}_j}$ denotes the average of $\acute{u}_i\acute{u}_j$. The symmetrical tensor $\overline{\rho \acute{u}_i \acute{u}_j}$, is known as the Reynolds stress tensor. Its dimension is that of a stress. The time average of (4.2) gives the Reynolds-averaged continuity equation:

$$\frac{\delta \bar{u}_i}{\delta x_i} = 0 \tag{4.5}$$

In this work only mean steady flows (U_i, P) are considered, but the influence of the small-scale turbulence on the time-averaged flow is of interest.

4.1.3 Spalart- Allmaras Model

Spalart-Allmaras Model is a single transport equation model solving directly for a modified turbulent viscosity. It is specifically designed for aerospace applications involving wallbounded flows on a fine, nearwall mesh. This model is economical for large meshes but performs poorly for three dimensional flows, free shear flows, flows with strong separation. Suitable for mildly complex external/internal flows and boundary layer flows under pressure gradient (e.g. airfoils, wings, airplane fuselage).

The one-equation model specially designed for aerospace application is given by the following equation:

$$\frac{\delta \hat{v}}{\delta t} + u_j\frac{\delta \hat{v}}{\delta x_j} = c_{b1}(1 - f_{t2})\hat{S}_v - \left[c_{w1}f_w - \frac{c_{b1}}{\kappa^2}f_{t2}\right]\left(\frac{\nu}{d}\right)^2 + \frac{1}{\sigma}\left[\frac{\delta}{\delta x_i}\left((\nu + \hat{v})\frac{\delta \hat{v}}{\delta x_i}\right) + c_{b2}\frac{\delta \hat{v}}{\delta x_i}\frac{\delta \hat{v}}{\delta x_i}\right] \tag{4.6}$$

and the turbulent eddy viscosity is computed from:

$$\mu_t = \rho\hat{\nu} f_v$$

where

$$f_{v1} = \frac{\chi^3}{\chi^3 + c_c^3} \tag{4.7}$$

$$\chi = \frac{\hat{\upsilon}}{\upsilon} \tag{4.8}$$

and ρ is the density, $\nu = \frac{\mu}{\rho}$ is the molecular kinematic viscosity, and μ is the molecular dynamic viscosity. Additional definitions are given by the following equations:

$$\hat{S} = \Omega + \frac{\hat{\upsilon}}{\kappa^2 d^2} f_{v2} \tag{4.9}$$

Where $\Omega = \sqrt{2W_{ij}}$ is the magnitude of the vorticity, *d* is the distance from the field point to the nearest wall, and

$$f_{v2} = 1 - \frac{\chi}{1+\chi f_{v1}} \qquad f_w = g\left[\frac{1+c_{w3}^6}{g^6 + c_{w3}^6}\right] \tag{4.10}$$

$$g = r + c_{w2}(r^6 - r) \tag{4.11}$$

$$r = \min\left[\frac{\hat{\nu}}{\hat{S}\kappa^2 d^2}, 10\right] \tag{4.12}$$

$$f_{t2} = c_{t3} exp(-c_{t4}\chi^2) \tag{4.13}$$

$$W_{ij} = \frac{1}{2}\left(\frac{\delta u_i}{\delta x_j} - \frac{\delta u_j}{\delta x_i}\right)$$

The boundary conditions are:

$$\hat{\nu}_{wall} = 0 \quad \hat{\nu}_{farfield} = 3\upsilon_\infty : to : 5\upsilon_\infty$$

The model constants are:

$c_{b1} = 0.1355 \quad \sigma = 2/3 \quad c_{b2} = 0.622 \quad \kappa = 0.41$

$c_{w2} = 0.3 \quad c_{w3} = 0.3 \quad c_{v2} = 7.1 \quad c_{t3} = 1.2 \quad c_{t4} = 0.5$

$$c_{w1} = \frac{c_{b1}}{\kappa^2} + \frac{1 + c_{b2}}{\sigma}$$

4.2. Physical modeling

Physical modeling is a step in which physical condition are applied to the models. It defines every environmental condition within the modeling domain that will be simulated during computation. All physical criteria expected to simulate need to be precisely defined in this step. The software has eight categories to define physical conditions. The physical conditions defined by this software are summarized in Table 4.1.

Table 4.1 Physical conditions for simulation

Physical Categories	**Assigned Physical Conditions**
Space, time and motion	Three-dimensional, Steady, Stationary
Materials	Gas, Air
Flow and energy	Segregated Flow Solver
Species	N/A
Turbulence Model	Spalart Allmaras
Radiation	N/A
Multiphase Flow	N/A
Combustion	N/A

Space, time and motion characterize the basic physical environment of the model. Space refers to spatial independent variables, which the model is encountering, which in this case is three-dimensional. Time is specified to be steady, which means physical time-step is not required. The solution will be solved at one physical condition, and one

physical time-step. Motion is assigned to be stationary as all mesh boundaries are motionless, and all reference frames are stationary.

Material assigned to the physical property is gas. Detail properties of air are specified including its dynamics viscosity, molecular weight, specific heat, thermal conductivity, and turbulent Prandtl number. The flow and energy solvers are offered in two options; coupled flow solver, and segregated flow solver. The Coupled flow model solves the conservation equations for mass and momentum simultaneously using a time- (or pseudo-time-) marching approach. It offers both explicit and implicit integration schemes that are first order and second order upwind. On the other hand, the segregated flow model solves the flow equations (one for each component of velocity, and one for pressure) in a segregated, or uncoupled, manner. The linkage between the momentum and continuity equations is achieved with a predictor-corrector approach. The segregated model offers central and Detached Eddy Simulation (DES) hybrid (second order upwind/central) integration scheme for both first order and second order upwind.

Coupled flow solver offers more robust and accurate method to solve compressible flow problems. It also costs more time and computation resources than segregated flow solver. Coupled flow model is recommended for compressible flow, or model with large body forces and energy. However, this simulation demands solver merely solving especially incompressible flow with a low turbulence level. The segregated flow is chosen to solve the problem since it is the most efficient, and is expected to provide satisfactory accuracy. It solves the governing equations with second order central integration scheme. A turbulence model must be chosen appropriately, as it influences boundary layers separations and transitions. There are four models available in the software; Spalart-Allmaras, k-Epsilon, k-Omega, and Reynolds Stress Transport. Spalart-Allmaras model is specially designed for aerospace industry application. It is suitable for application in which its boundary layer separation is not dominant. The k-Epsilon models offer good balance between robustness, cost and accuracy. It is suitable for complex turbulent situation. And it is the most expensive models in terms of required computation. In this analysis along with Spalart-Allmaras, both K-Epsilon and K-Omega models are also used, but Spalart-Allmaras model gives the most consistent results. Considering the requirement of computational time and resources and comparing the results with other available turbulence models, Spallart- Allmaras is chosen for this investigation.

After physical model is being set, input values must be entered in order to proceed the analyzing step as shown in Table 4.2.

Table 4.2 Input parameters for physical modeling setup

Input Condition	**Input Values**
Dynamic Viscosity of air	1.85×10^{-5} Pa-s
Reference Pressure	101325 Pa
Static Pressure (Initial Condition)	0 Pa
Static Temperature(IC)	300 K
Air Density	1.184 kg/m3
Initial Velocity	According to Reynolds Number
Turbulent Viscosity Ratio	10
Flow Direction	According to Angle of Attack

Other properties of air such as molecular weight, specific heat and turbulent Prandtl number are set to the default values. It is considered reasonable because at incompressible flow condition, these values are close or unchanged from standard sea level values, which are provided by the software. Initial velocity is set as the velocity corresponding to the Reynolds Number for inlet velocity. Turbulent viscosity ratio is approximated to be 10 as an initial value. By choosing turbulent suppression option, the program will automatically calculate transition boundary layer, and transition distance. Flow direction specification depends on angle of attack. The simulation runs at different attack angles which are the same range as the experiment for each aircraft model.

4.3 Running simulations

After setting proper physical and initial conditions, simulations are initiated. This finite volume software produces a residuals plot for each simulation, which graphically display products from the solving equations versus iteration step in log-log scale.

Residual displays are good for judging convergence of simulations. Good convergence is judged by having all residuals to be steady and/or drop by some order of magnitude.

However, sometimes if initial conditions match perfectly for solution, residuals may drop only slightly, and stay level throughout the simulation. Sometimes a solution may not converge and oscillations occur, which might be due to insufficient number of cells. Fig. 4.1 shows convergence history of residuals. Once the plotted results not changes with farther iteration; indicates that convergence has occurred. It is important to judge convergence with care in order to obtain correct results.

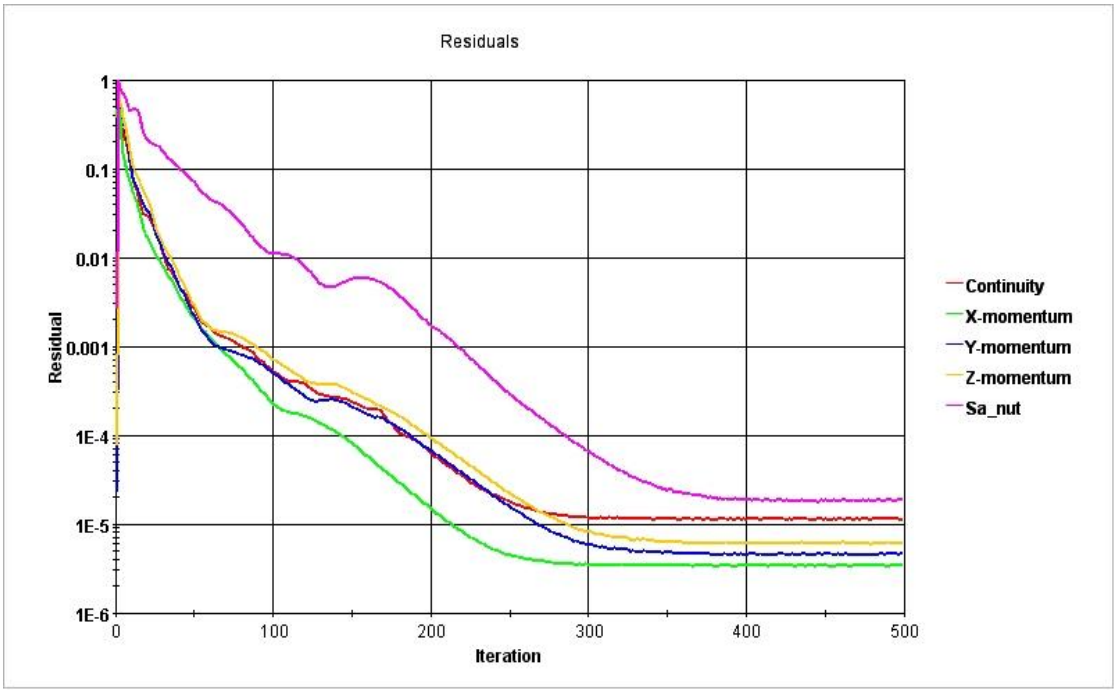

Fig. 4. 1 Residual plot

4.4 Mesh Sensitivity Analysis

The mesh sensitivity analysis is performed for airfoiled fuselage model observing the alteration of the calculated values of Lift Coefficient (C_L), with increasing number of mesh elements. Airfoiled fuselage with $2°$ wing angle and $0°$ angle of attack is taken. Tests are performed from nearly 67000 elements to 450000 elements. Computational resources circumscribed the number of cells. For this analysis Core-2-duo processor with 4GB RAM is used. As three dimensional volume meshing requires very high memory, so analysis is performed with relatively coarse meshes.

Values of Lift Coefficient (C_L), for different number of mesh elements is shown in Fig. 4.2. It is well noticeable that, the value of C_L for this specific case cannot be improved

significantly by taking higher number of elements above 400000. However, in this analysis the model is solved for different angle of attack and wide range of Reynolds numbers. At higher angle of attack and Reynolds numbers massive flow separation occurs form the aircraft surfaces. To ensure computational accuracy, high mesh density volume control element is used around the fuselage model, which significantly increases the number of cells in those cases.

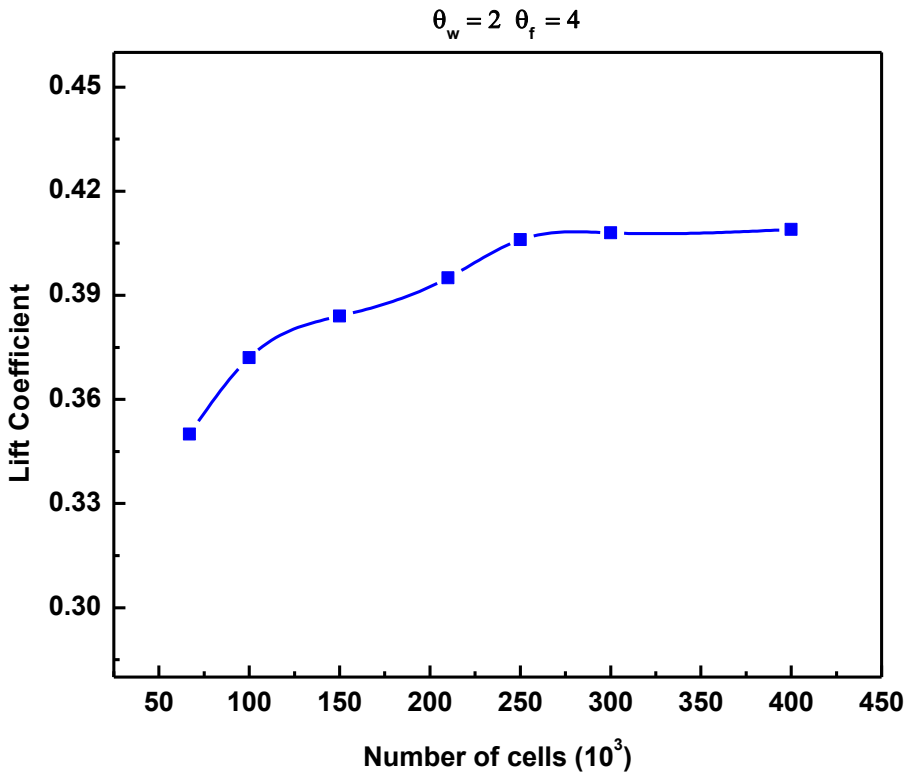

Fig. 4.2 Mesh sensitivity analysis for Lift Coefficient

4.5 Flow Chart of Overall Solution Methodology

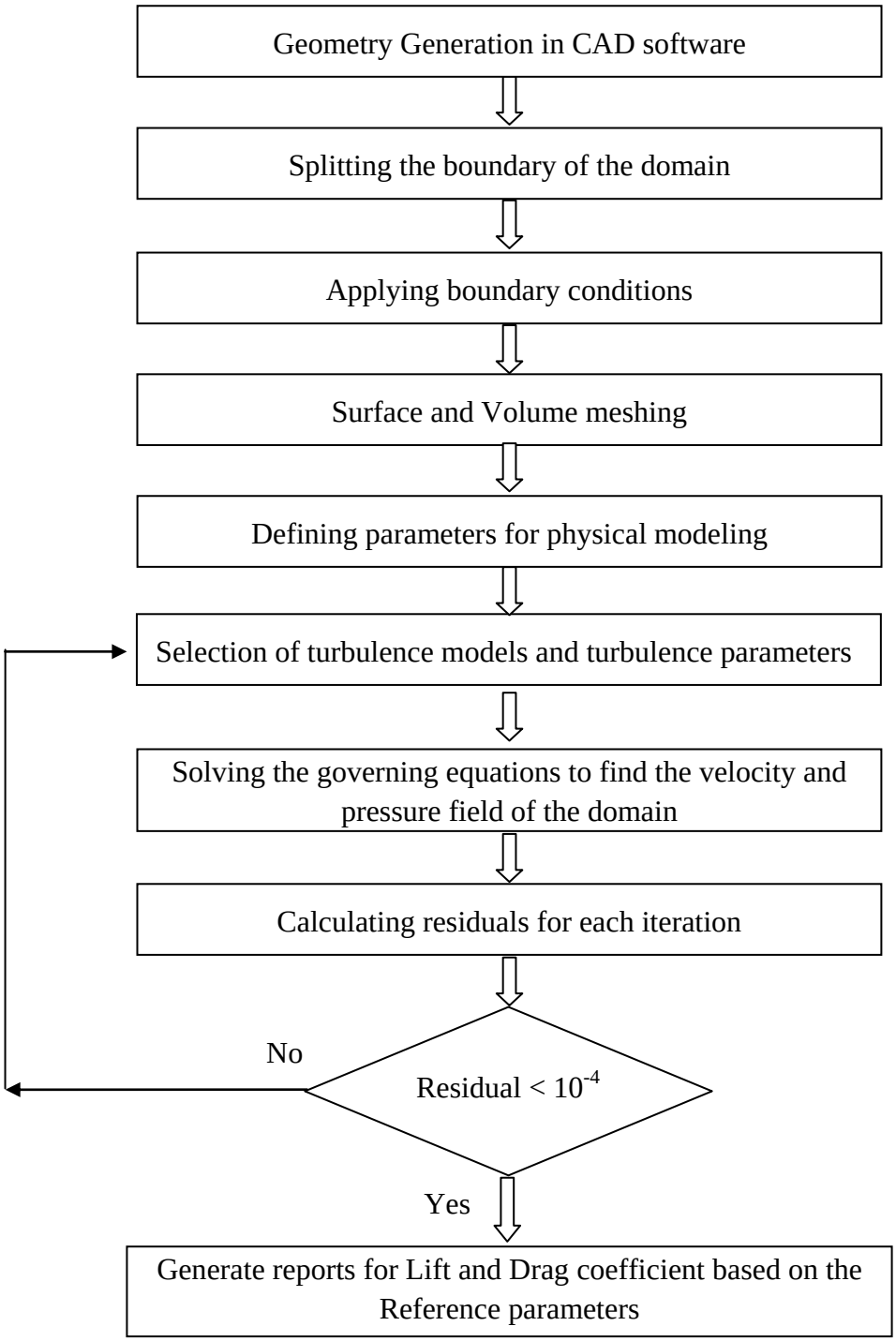

CHAPTER 5
RESULT AND DISCUSSION

This chapter provides the Lift and Drag Coefficients, Lift to Drag Coefficient ratios of the both airfoiled and circular fuselage models. The developed model used in this analysis is validated by comparing the calculated values of C_L and C_D for the airfoiled fuselages with the available experimental data. Later C_L , C_D and L/D ratios for different fuselage profiles covering the range of angle of attack and wing angles and of different Reynolds number are determined. For each combination of angle of attack of the fuselage and the wing Lift Coefficient vs. Reynolds No. curves, Drag Coefficient vs. Reynolds No. curves and L/D vs. Reynolds No. curves are drawn. For comparison among the models the curves at a particular angle of attack for all the models are drawn in a single graph.

5.1 Model Validation

Analysis is started with the validation of a two dimensional model of NACA 2412 airfoil. Lift and drag coefficients for NACA 2412 airfoil are determined by finite volume software using Spalart-Allmaras as viscous model for Re=3.1×10^6 and compared with the experimental data available at Theory of wing section [30]. Fig. 5.1 and Fig. 5.2 shows the comparisons of experimental and numerical values of lift and drag coefficients. As in the two dimensional case, the computational data are in well harmony with the experimental data then the three dimensional finite volume model of both airfoiled and circular sectioned fuselages are developed. In the next section, for a wide range of Reynolds number, angles of attack, and at different wing angle, lift and drag coefficients are plotted with the experimental data [28] to show the comparison. From these graphs it is observed that, the nature of numerical values of the lift and drag coefficients with the Reynolds number conforms to the experimental data, although in some of the cases larger discrepancies are noticeable. All the data are given in the appendix section.

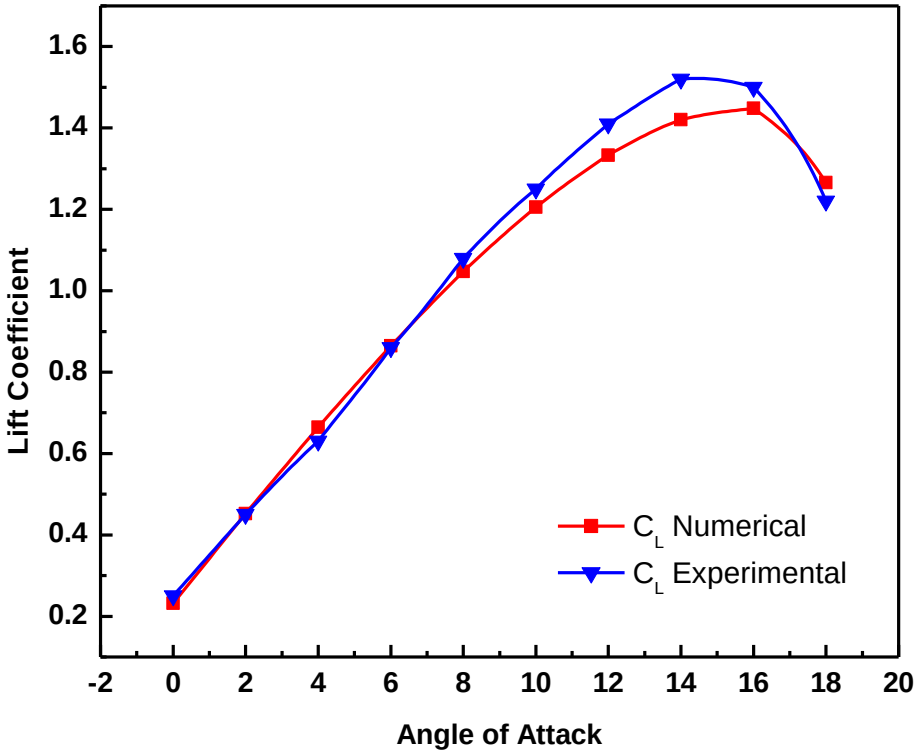

Fig. 5.1 Comparison of numerical Lift Coefficient of NACA 2412 airfoil with the experimental data

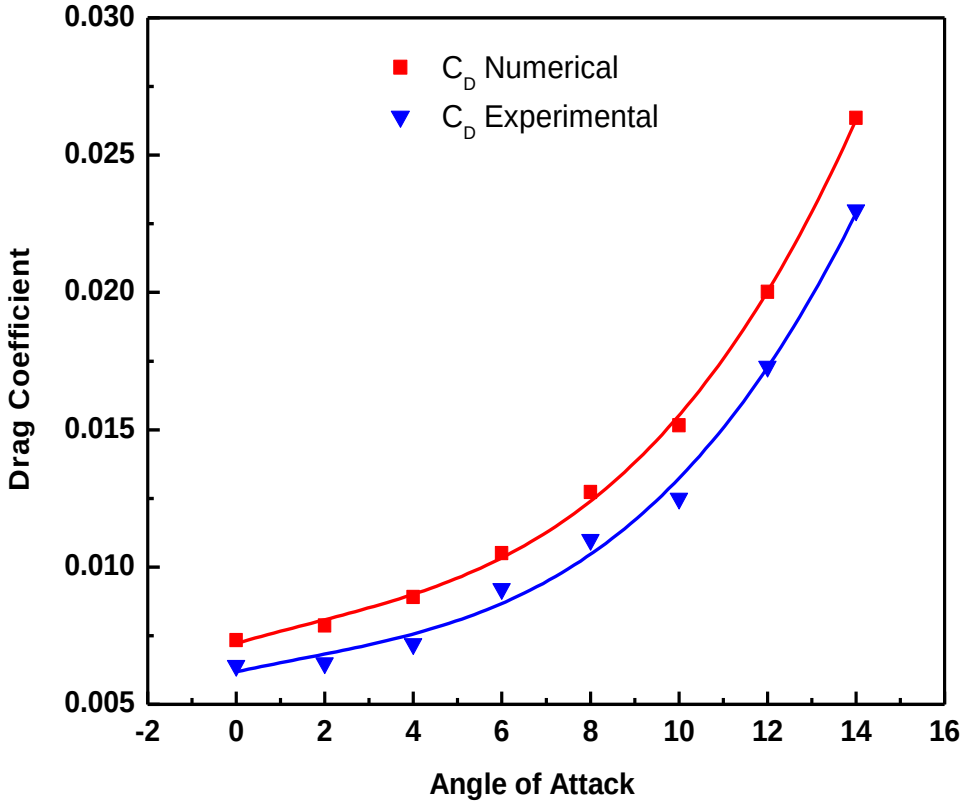

Fig. 5.2 Comparison of numerical Drag Coefficient of NACA 2412 airfoil with the experimental data

In this thesis, the model is solved using Reynolds Averaged Navier-Stokes (RANS) equations and the flow contains both laminar and turbulent region. P. Silisteanu et. el [31] states, RANS equations overpredicts the airplane skin-friction and drag coefficients if the flow contains laminar regions. Moreover RANS models cannot predict forces on the laminar to turbulent transition zone. For the precise prediction of the drag transition models are recently developed [30], which are not included in the currently available version of this simulation software. Main reason of airfoil drag is shear forces at wall. So prism layer meshing scheme is used to ensure some grid points within the viscous sub-layer to capture the drag. But the greater number of prism layer causes a myriad number of cells which goes beyond the capacity of available computational resources. So drag coefficients with reasonable discrepancy are accepted for the simulation. Another reason of errors in the numerical results could be, the actual models that were run in the wind tunnel experiment could have variances from the computer aided design (CAD) models that are used in this simulation.

5.2 Experimental Conditions

Numerical data is validated with the available experimental data [28]. That experiment was carried out in a 700mm×700mm closed circuit wind tunnel as shown in Fig. 5.3. The model is placed in open air, so atmospheric conditions are applicable on this analysis.

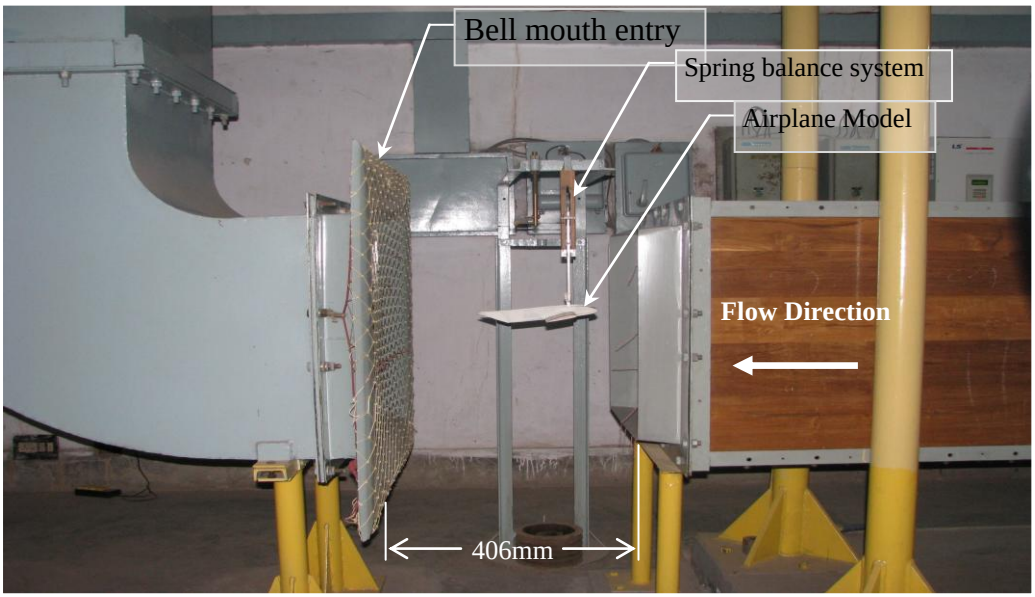

Fig. 5.3 The model in the test section of the 700mm × 700mm closed circuit Wind Tunnel

5.3 Lift and Drag Coefficients Calculation

The whole investigation is carried out for different wing angle (relative to fuselage) and angle of attack configuration. Wing angle for both type of model is 2^o, 4^o and 6^o. Lift and drag coefficients are calculated for a range of angle of attack from 0^o to 16^o at every 4^o interval. So for a fixed wing angle setup, angle of attack changes from 0^o to 16^o.

Before going to discuss the results some other points related to aircraft maneuvering need to mention. As during takeoff lift force must be greater than the weight of the aircraft, and high lift coefficient is required, and to overcome the drag high engine thrust is needed. During level flight the weight of the aircraft must be balanced by the generated lift force. If the air speed increases the lift coefficient need to decrease to keep the balance. Another point is- the level flight covers maximum portion of flight duration so fuel economy is also a concern. If during this, aircraft moves in a lower speed, in that case it must fly at high angle of attack which causes high induced drag. So during level flight maximum lift to drag ratio is an important parameter for fuel economy. Another point to maintain high L/D ratio is flying with minimum drag. But this minimum drag divides the total drag into induced drag - which decreases in proportion to the square of the speed - and all the-remainder of the drag increases in proportion to the square of the speed. Again during landing as the speed of the aircraft decreases so to keep the plane floating lift coefficient must be increased which is done by increasing angle of attack [32].

In the next section, corresponding to a fixed wing angle results for different angles of attack are described.

5.3.1 Relative angle between fuselage and wing, $\theta_w = 2^o$

For a fixed wing angle $\theta_w = 2^o$, effect of different angle of attacks are described in the following subsections.

5.3.1(i) $\theta_w = 2^o$ and $\theta_f = 0^o$

Fig. 5.4(a) shows the lift coefficient vs. Reynolds number curve for both experimental and numerical results for both airfoiled and circular cross-section fuselages. Numerical values conform quite well to the corresponding experimental data. As the airfoiled fuselage contributes to the overall lift so, this model has higher lift coefficient than the

circular one. From the Fig. 5.4(b) it is found that drag coefficients for airfoiled fuselages are higher primarily due to the induced drag. From the numerical results, it is found that takeoff speeds for airfoiled and circular fuselages are 80 km/h (Re = 1.6×10^5) and 85 km/h (Re = 1.65×10^5) respectively. It is also found that air speed above 105 km/h lift coefficient changes precipitously for both type of model and after 90 km/h (Re = 1.6×10^5) drag coefficient falls rapidly. As the angle of attack is 0^o, separation causes drag crisis at 90 km/h but lift crisis at higher air speed of 105 km/h. The lift to drag ratio as shown in Fig. 5.4(c) is higher for circular cross-section fuselage. Airfoiled sections yield lower L/D ratio mainly due to the tip vortices generated at both side of the finite fuselages. These tip vortices reduce lift coefficient and induced drag increases total drag, their cumulative effect results lower L/D ratio for airfoiled fuselages.

5.3.1(ii) $\theta_w = 2^o$ and $\theta_f = 4^o$

Fig. 5.5(a) shows experimental and numerical values of lift coefficients for both airfoiled and circular cross section fuselages at different Reynolds numbers. The trend of the numerical results matches well with the experimental results although numerical values are lower than the experimental. From the numerical results the takeoff speed for both types of fuselages could be approximately 65 km/h (1.30×10^5). Lift coefficients falls rapidly after Re = 1.40×10^5. Fig. 5.5(b) shows the variation of drag coefficients with the Reynolds number. Similar to lift coefficient, drag coefficient also decrease at air speed of 70 km/h. With the increase in flow angle, separation commences earlier and decreases the lift coefficient and increases the pressure drag with the Reynolds number. Lift to drag ratio for airfoiled fuselage is lower than the circular one due to generated tip vortices at airfoiled fuselage.

5.3.1(iii) $\theta_w = 2^o$ and $\theta_f = 8^o$

Fig. 5.6(a) shows the lift coefficients for both the model matches well with the experimental data. But at Fig. 5.6(b) drag coefficients have greater discrepancy with the experimental results. As the separation increases with the increase in Reynolds number numerical prediction become somewhat less accurate. Lift crisis occurs at approximately 75 km/h (Re=1.75×10^5). Lift to drag ratio of airfoiled fuselage is lower in both the cases

of experimental and numerical analysis. At high air speed lift and drag coefficient both decreases results lower L/D ratio.

5.3.1 (iv) $\theta_w = 2^o$ and $\theta_f = 12^o$

At this high angle of attack, at lower Reynolds numbers very high lift forces are generated but with the increasing air speed the lift coefficient falls rapidly, which is shown lift coefficient vs. Reynolds number curve in Fig. 5.7(a). Up to Re = 1.55×10^5 lift force generated by airfoiled fuselage is higher than circular one but subsequent flow separation and tip vortices generated at finite length airfoiled fuselages reduces the lift coefficient. At high Reynolds number drag coefficients fall very rapidly and airfoiled fuselage has lower drag than circular fuselage at this high angle of attack. Lift to drag ratio of airfoiled fuselages is higher than the circular fuselage model as shown in Fig. 5.7(c).

5.2.1(v) $\theta_w = 2^o$ and $\theta_f=16^o$

At this angle of attack very high lift forces are generated at low Reynolds number but it falls immediately with the increasing speed as shown in Fig. 5.8(a). Flow separation is dominant in this case which increases drag forces as well but large values of lift coefficients supersede the effect of high drag results higher overall L/D ratio. In comparison of both types of fuselages, greater L/D ratio is found from airfoiled section than the circular section fuselage.

5.3.2 Relative angle between fuselage and wing, $\theta_w = 4^o$

For a fixed wing angle $\theta_w = 4^o$, effect of different angle of attack are described in the following subsections.

5.3.2(i) $\theta_w = 4^o$ and $\theta_f = 0^o$

In Fig. 5.9(a) numerical values of lift coefficient matches with the experimental values for airfoiled fuselage but for circular fuselage causes greater discrepancy. Takeoff speed for airfoiled and circular fuselages could be 60 km/h (Re = 1.2×10^5) and 75 km/h (Re = 1.5×10^5) respectively. Numerical values of drag coefficient causes fluctuations with the Reynolds number for airfoiled fuselages but values of circular fuselages are

possessing similarity with the experimental data. Flow separation at high Reynolds number reduces the lift coefficient and increases the drag for both type of fuselages but airfoiled fuselages have lower L/D ratio as shown in Fig. 5.9(c).

Other investigated combinations are-

5.3.2(ii) $\theta_w = 4^o$ and $\theta_f=4^o$

5.3.2 (iii) $\theta_w = 4^o$ and $\theta_f=8^o$

5.3.2 (iv) $\theta_w = 4^o$ and $\theta_f=12^o$

5.3.2 (v) $\theta_w = 4^o$ and $\theta_f=16^o$

5.3.3 Relative angle between fuselage and wing, $\theta_w = 6^o$

For a fixed wing angle $\theta_w = 6^o$, effect of different angle of attack are described in following subsections.

5.3.3 (i) ($\theta_w = 6^o$ and $\theta_f=0^o$

5.3.3(ii) $\theta_w = 6^o$ and $\theta_f=4^o$

5.3.3(iii) $\theta_w = 6^o$ and $\theta_f=8^o$

5.3.3 (iv) $\theta_w = 6^o$ and $\theta_f=12^o$

All the above combination shows the similar pattern in the lift and drag coefficients. The combination of $\theta_w = 6^o$ and $\theta_f=4^o$ of airfoiled fuselages shows high lift to drag ratio at the operating range. Based on the earlier mentioned points, it can be said that $\theta_w = 6^o$ and $\theta_f=4^o$ combination is a good attitude during level flight. In some other combinations where at low Reynolds number high lift coefficient is found can be chosen during takeoff.

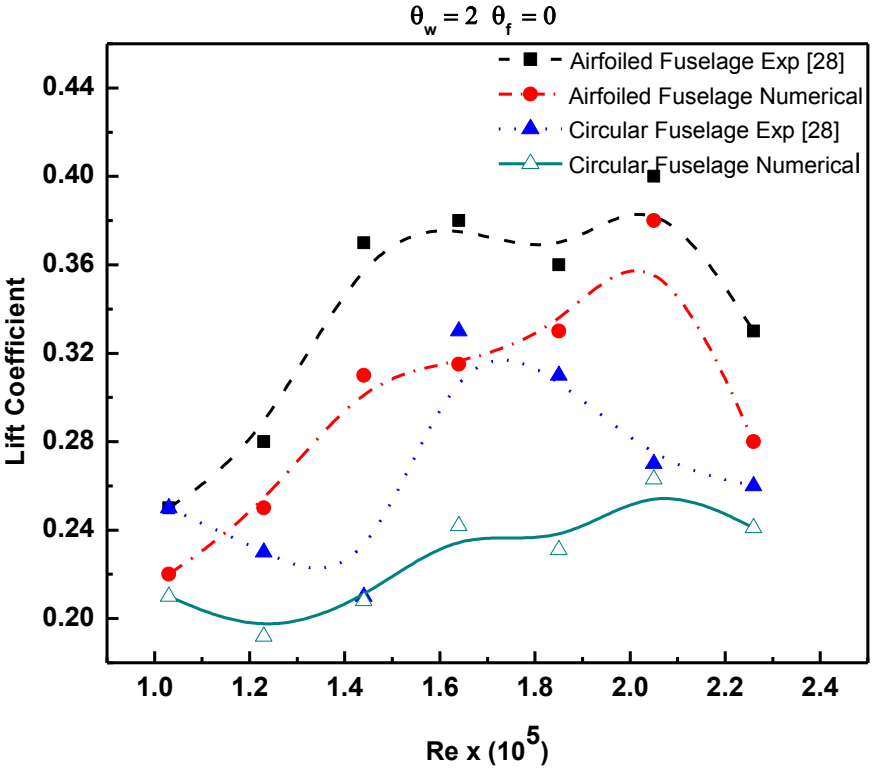

Fig. 5.4(a) Lift Coefficient vs. Reynolds number curves for $\theta_w = 2^o$ and $\theta_f=0^o$

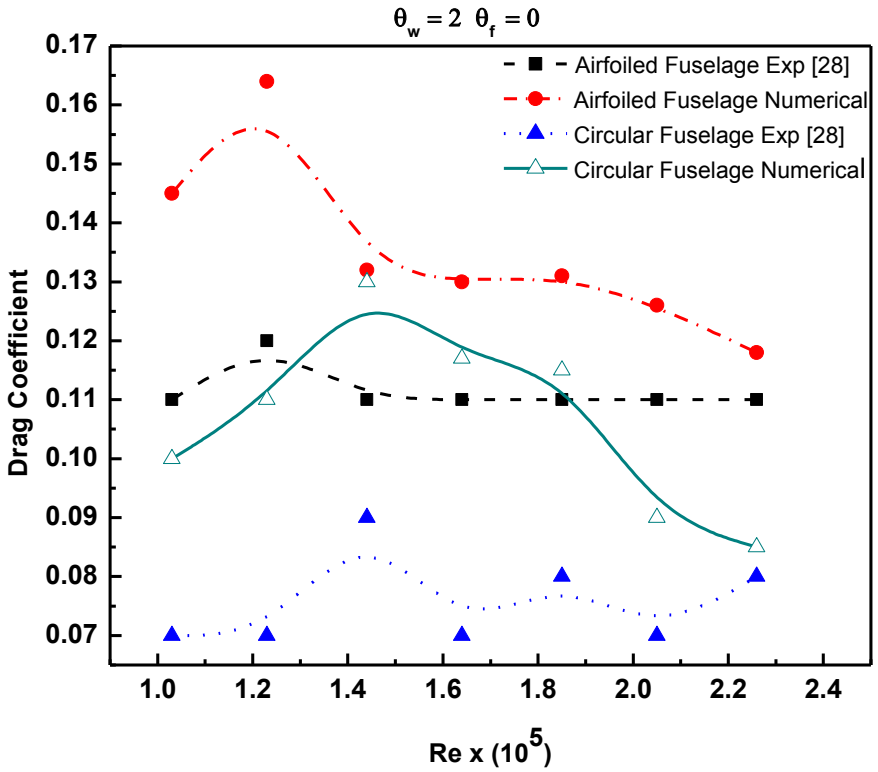

Fig. 5.4(b) Drag Coefficient vs. Reynolds number curves for $\theta_w = 2^o$ and $\theta_f=0^o$

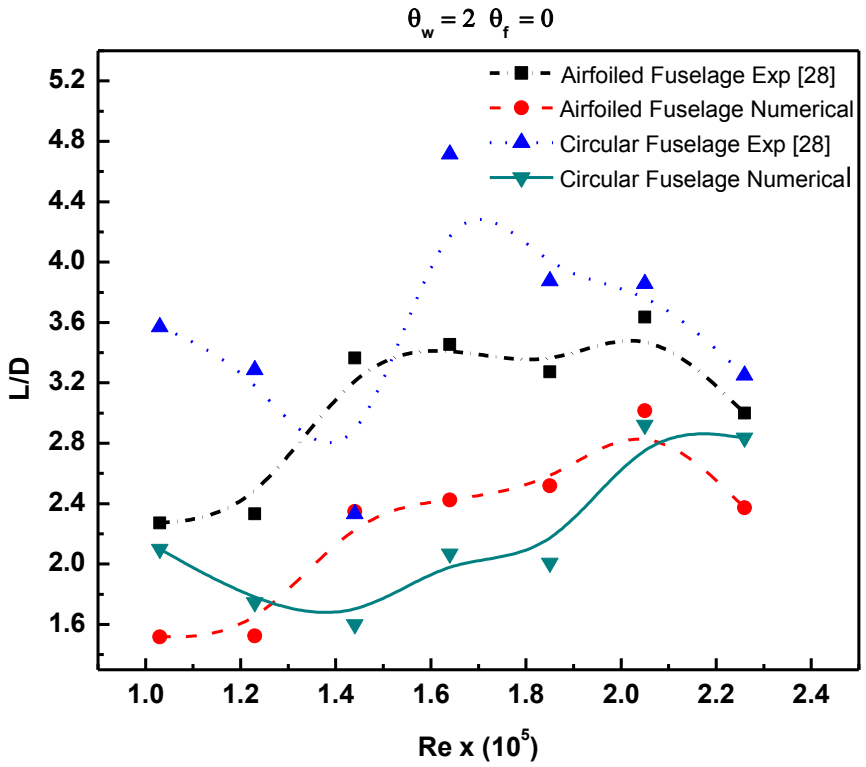

Fig. 5.4(c) L/D vs. Reynolds number curves for $\theta_w = 2^o$ and $\theta_f=0^o$

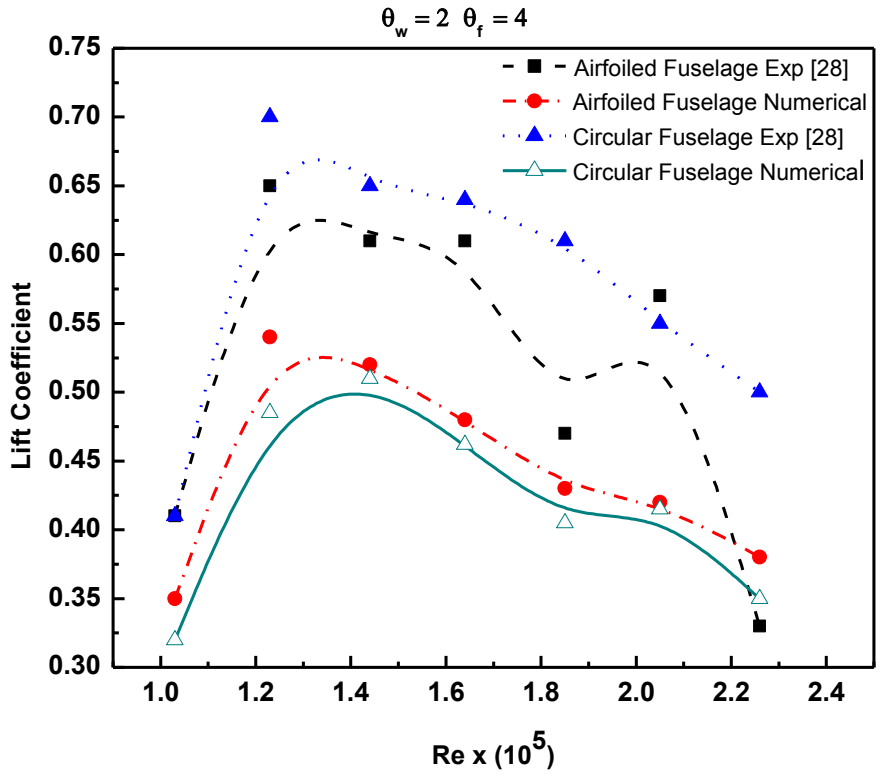

Fig. 5.5(a) Lift Coefficient vs Reynolds number curve for $\theta_w = 2^o$ and $\theta_f=4^o$

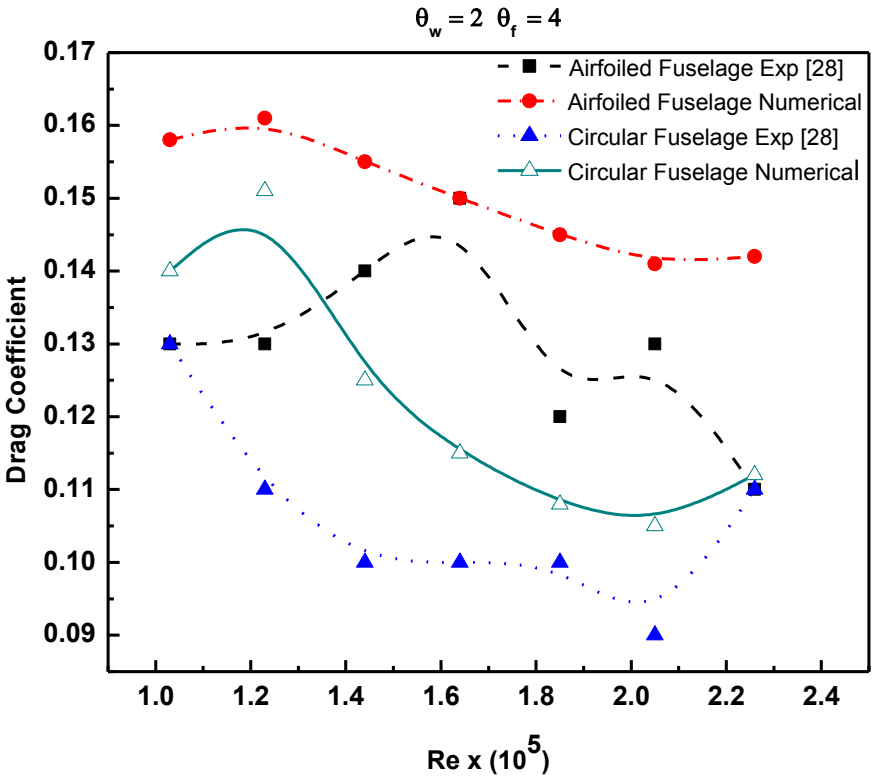

Fig. 5.5 (b) Drag Coefficient vs. Reynolds number curves for $\theta_w = 2^o$ and $\theta_f = 4^o$

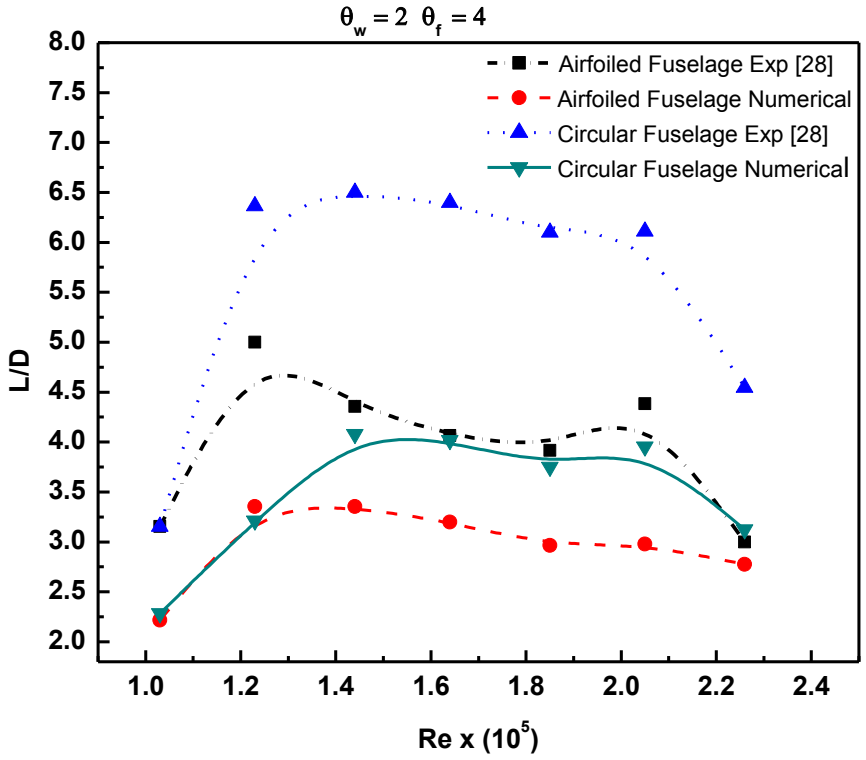

Fig. 5.5(c) L/D vs. Reynolds number curves for $\theta_w = 2^o$ and $\theta_f = 4^o$

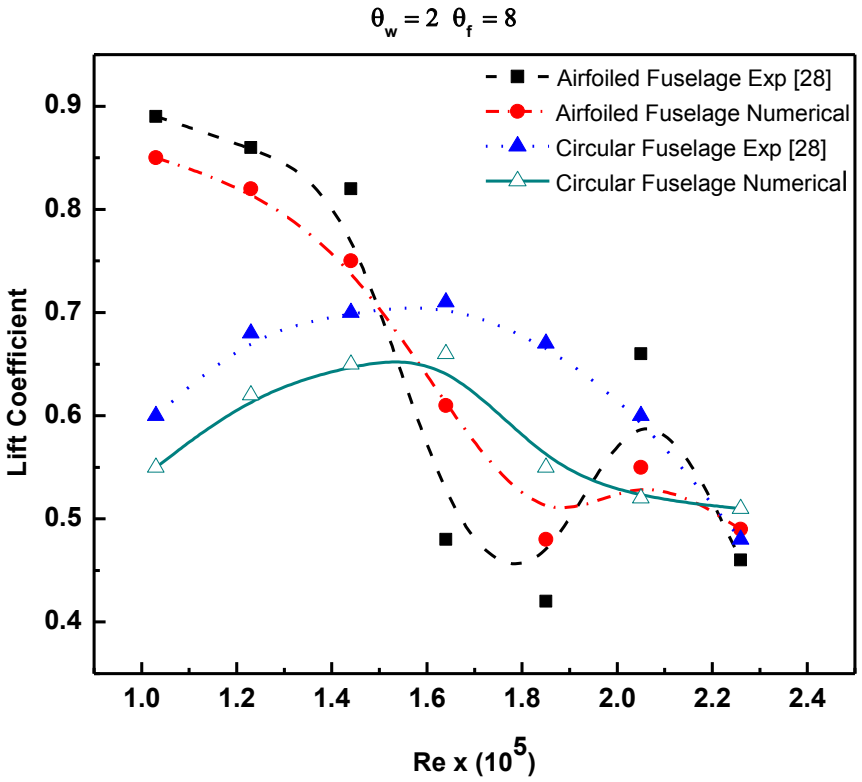

Fig. 5.6(a) Lift coefficient vs. Reynolds number for θ_w=2^o, θ_f =

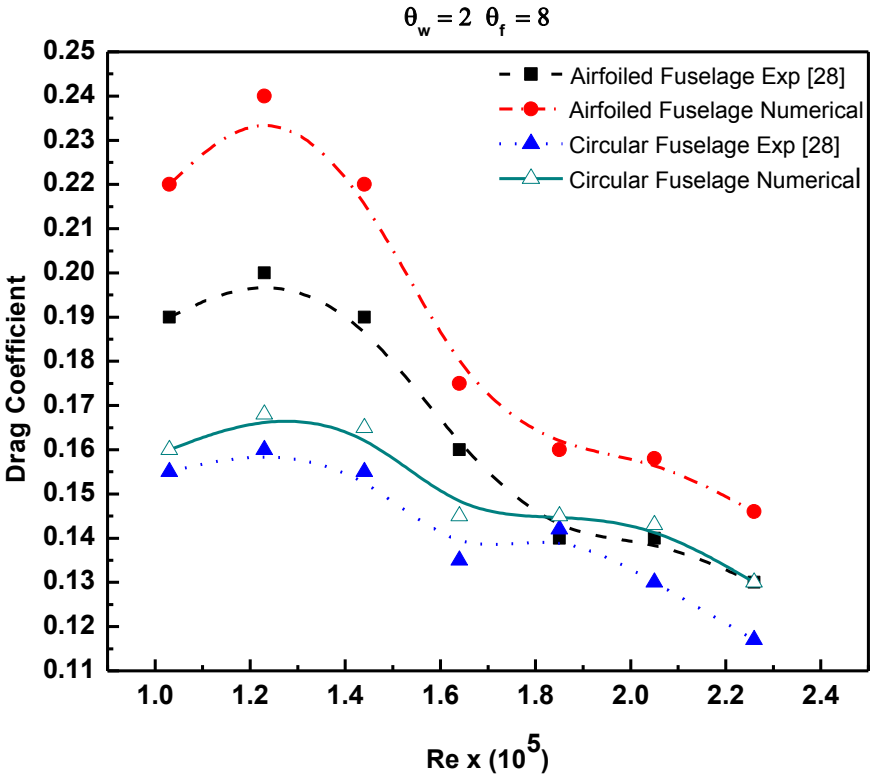

8^o

Fig. 5.6(b) Drag Coefficient vs. Reynolds number curve for θ_w=2^o, θ_f = 8^o

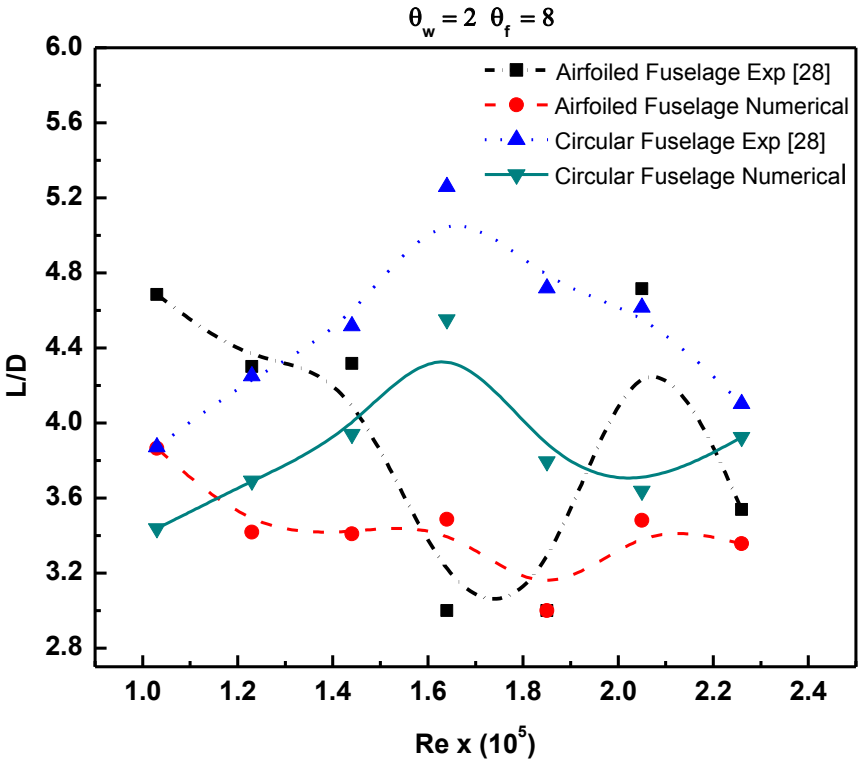

Fig. 5.6(c) L/D vs. Reynolds number curve for θ_w=2^o, θ_f =

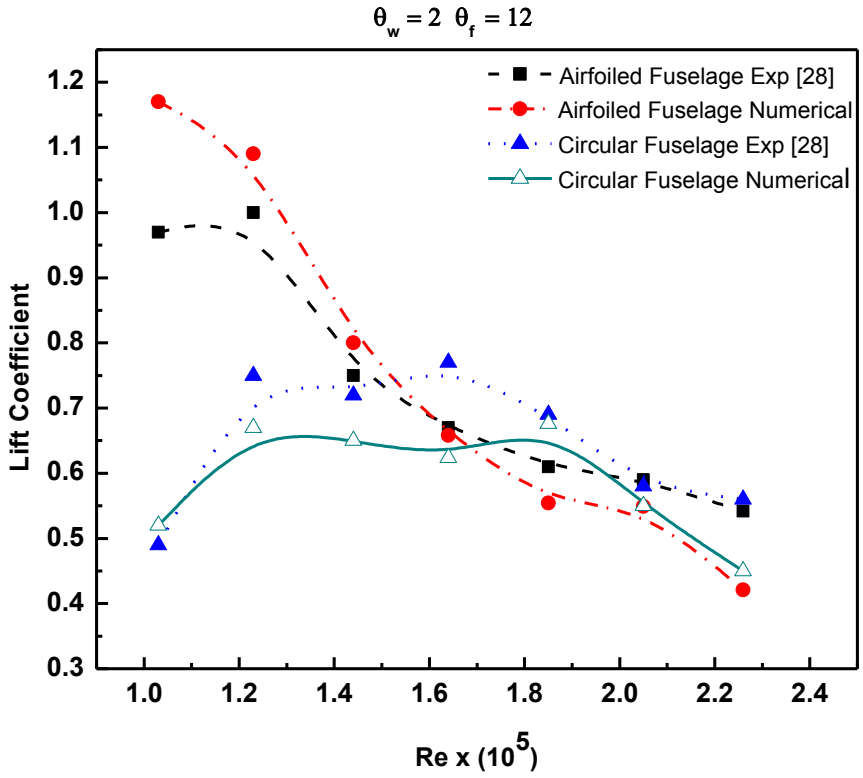

8^o

Fig. 5.7(a) Lift Coefficient vs. Reynolds number curve for θ_w=2^o, θ_f = 12^o

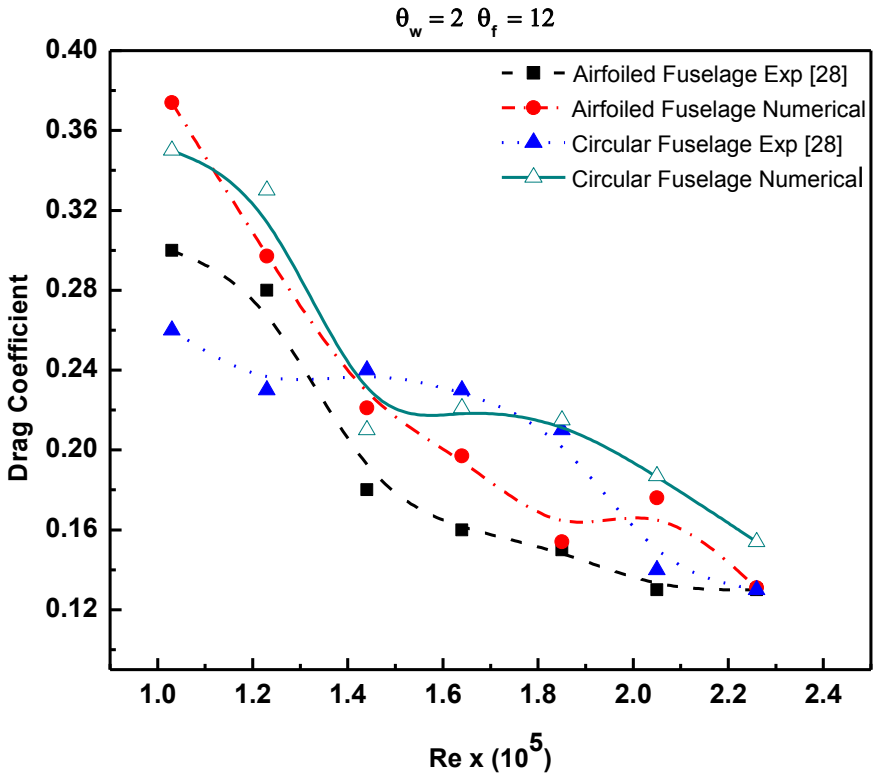

Fig. 5.7(b) Drag Coefficient vs. Reynolds number curve for θ_w=2^o, θ_f = 12^o

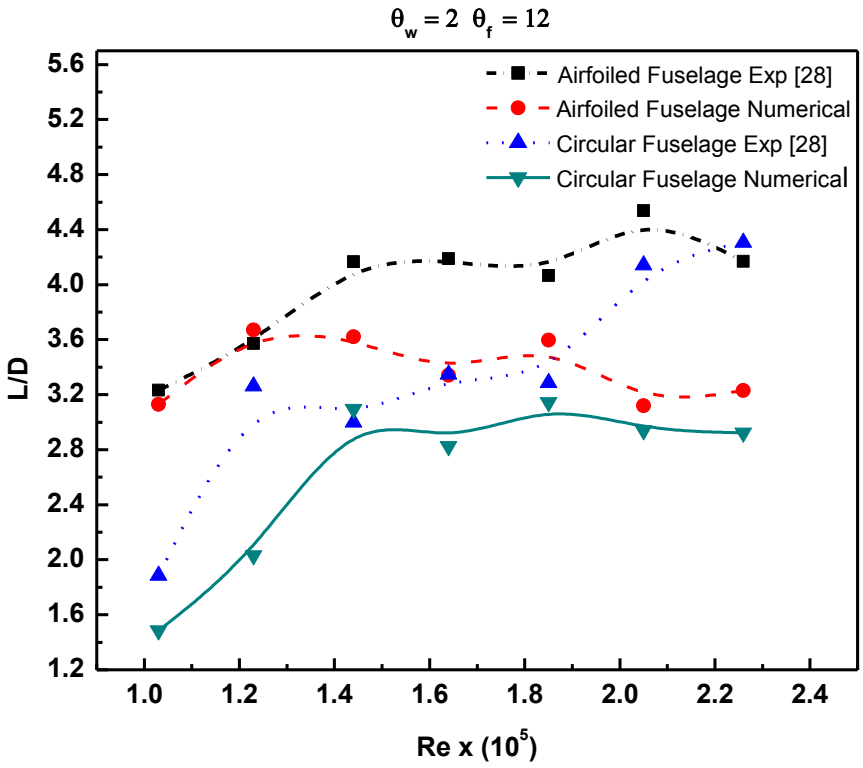

Fi

g. 5.7(c) L/D vs. Reynolds number curve for $\theta_w=2^o$, $\theta_f = 12^o$

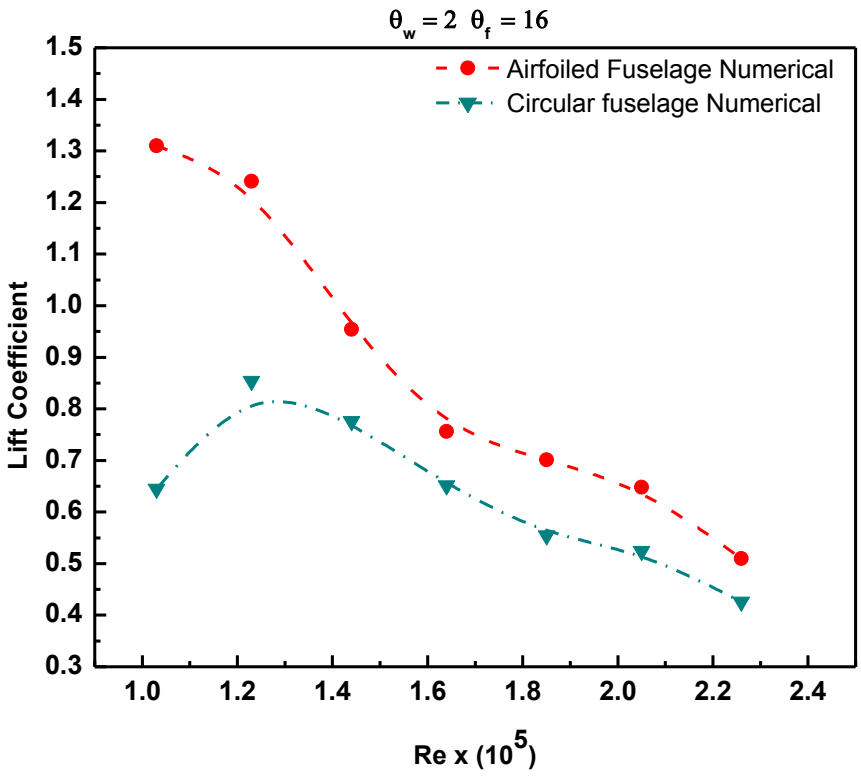

Fi

g. 5.8(a) Lift Coefficient vs. Reynolds number curve for $\theta_w=2^o$, $\theta_f = 16^o$

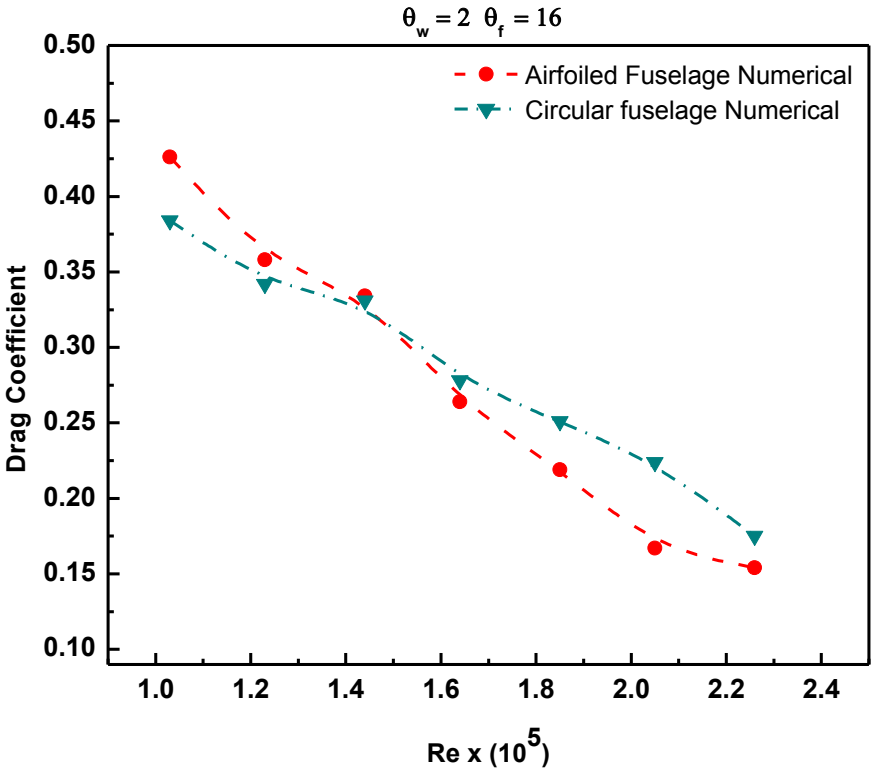

Fig. 5.8(b) Drag Coefficient vs. Reynolds number curve for $\theta_w=2^o$, $\theta_f = 16^o$

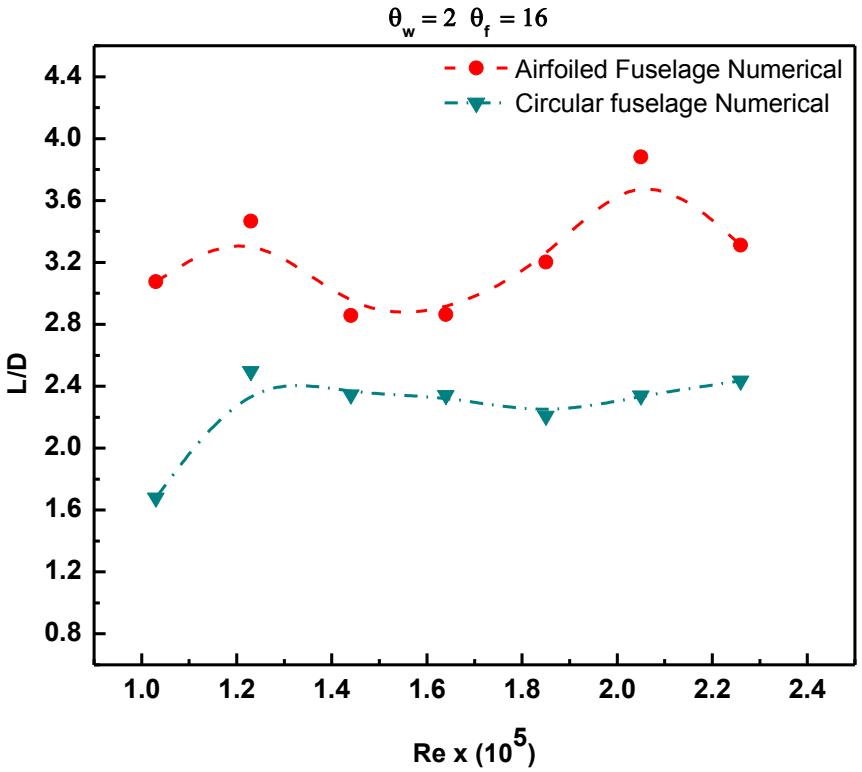

Fig. 5.8(c) L/D vs. Reynolds number curve for $\theta_w=2^o$, $\theta_f = 16^o$

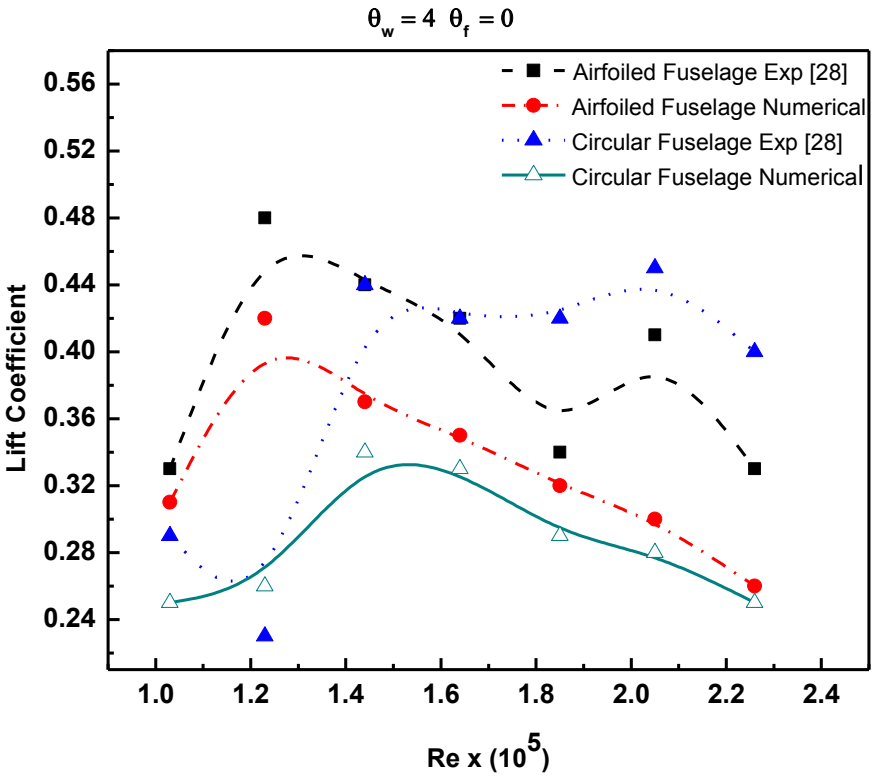

Fig. 5.9(a) Lift coefficient vs Reynolds number curve for θ_w=4^o, θ_f = 0^o

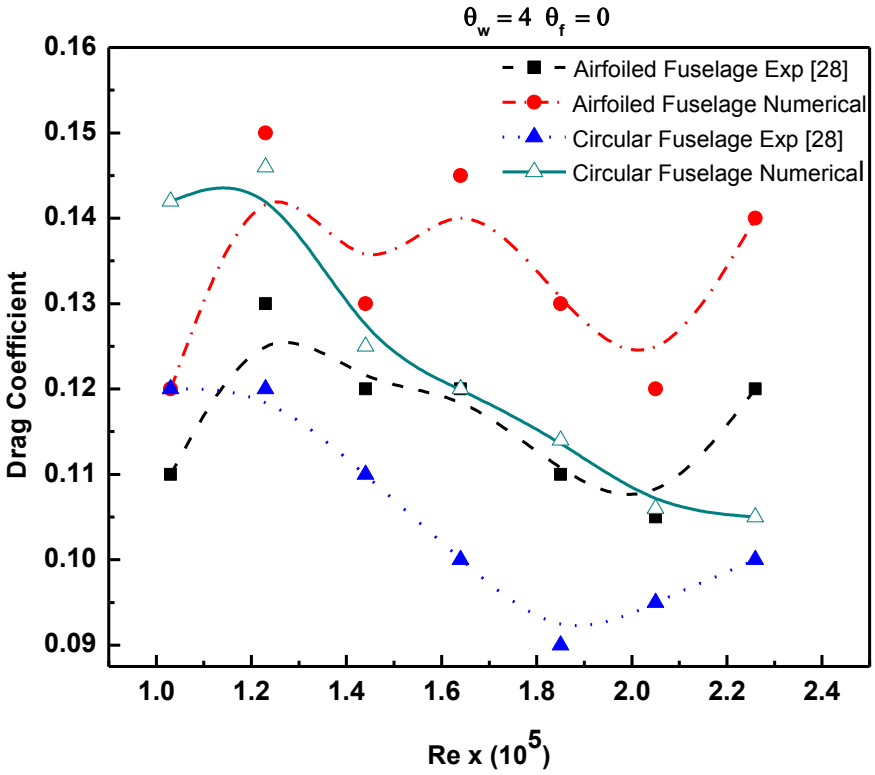

Fi

g. 5.9(b) Drag coefficient vs Reynolds number curve for θ_w=4^o, θ_f = 0^o

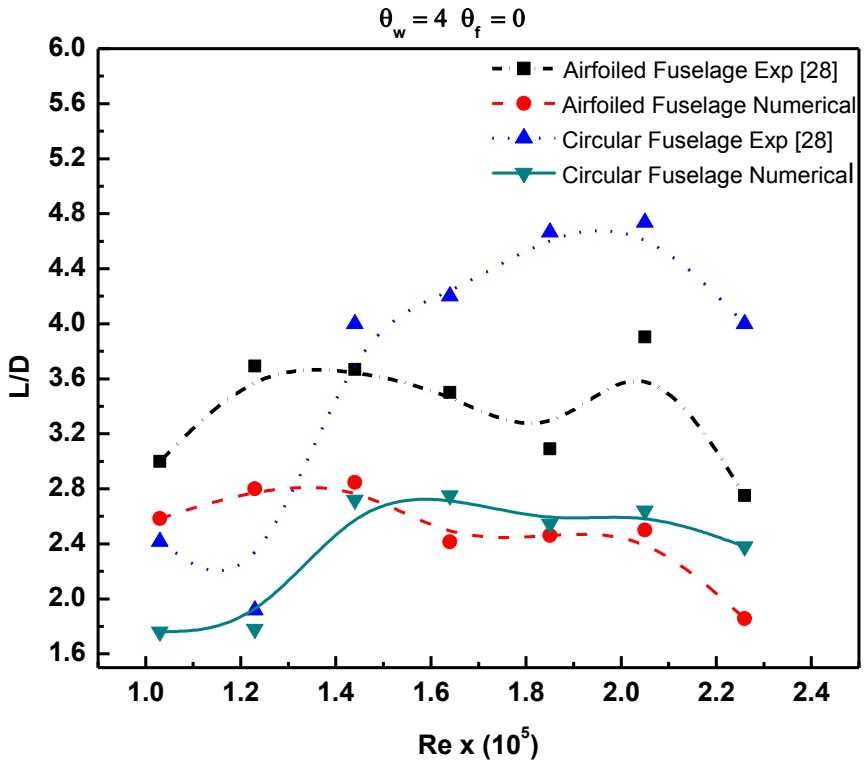

Fig. 5.9 (c) L/D vs Reynolds number curve for θ_w=4^o, θ_f = 0^o

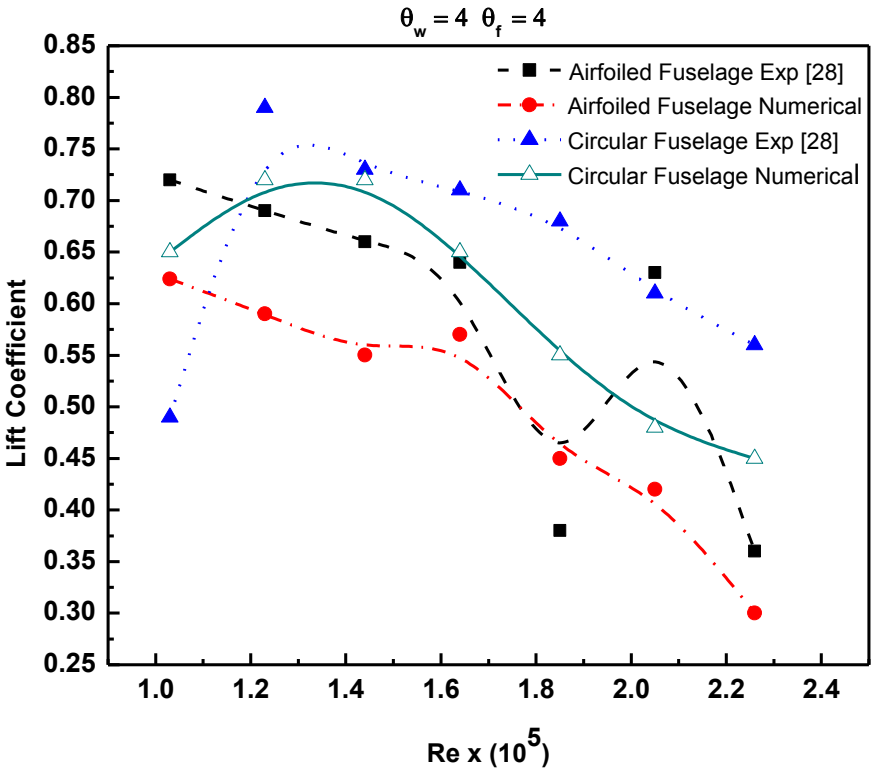

Fig. 5.10 (a) Lift coefficient vs. Reynolds number curve for θ_w=4^o, θ_f = 4^o

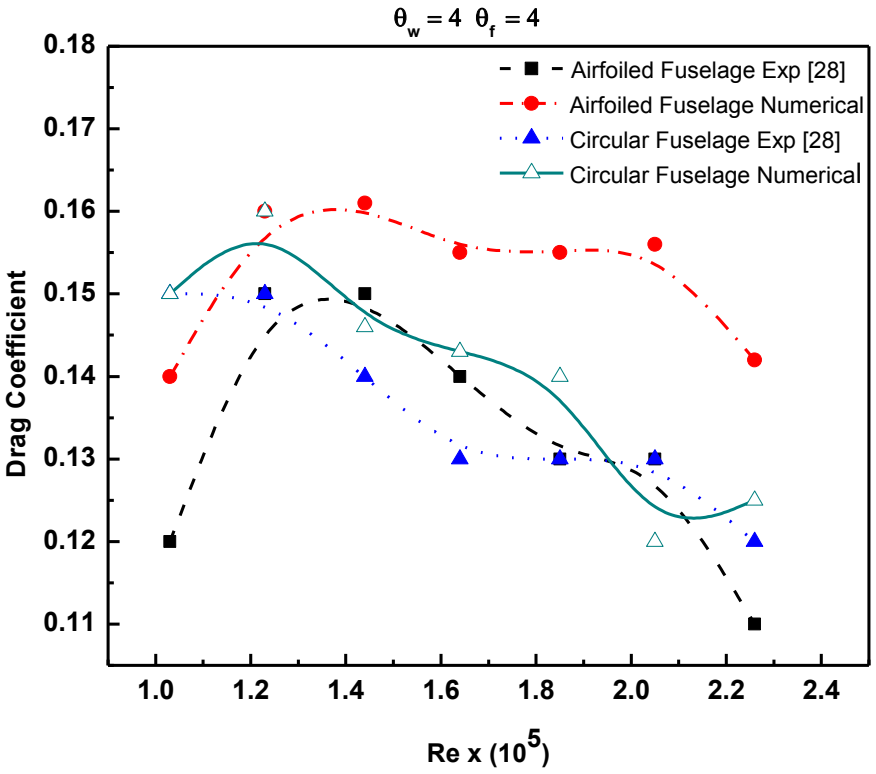

Fig. 5.10(b) Drag coefficient vs Reynolds number curve for θ_w=4^o, θ_f = 4^o

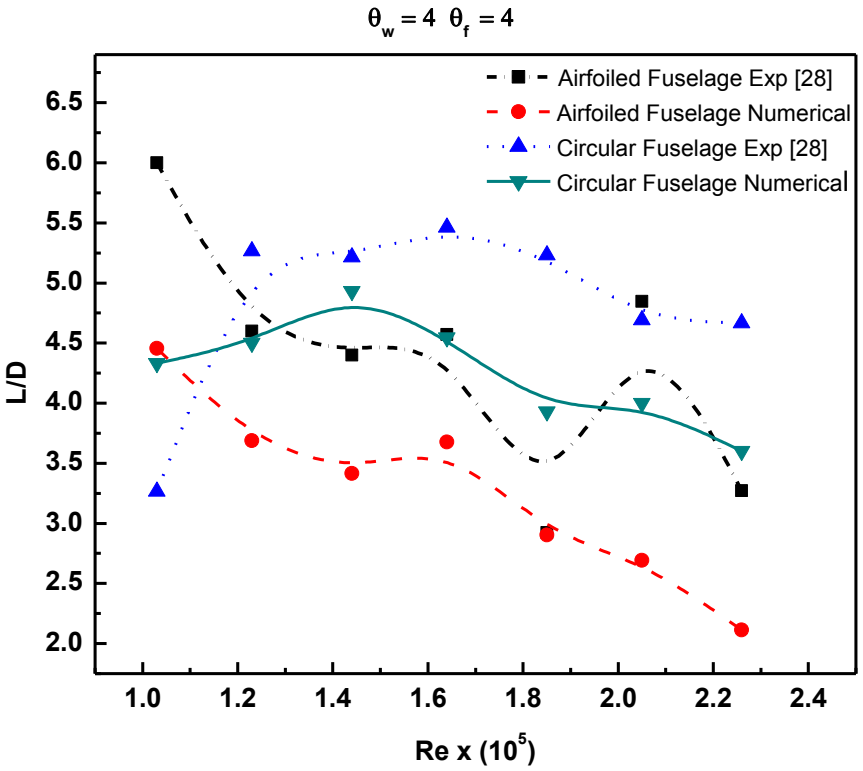

Fig. 5.10(c) L/D vs Reynolds number curve for θ_w=4^o, θ_f = 4^o

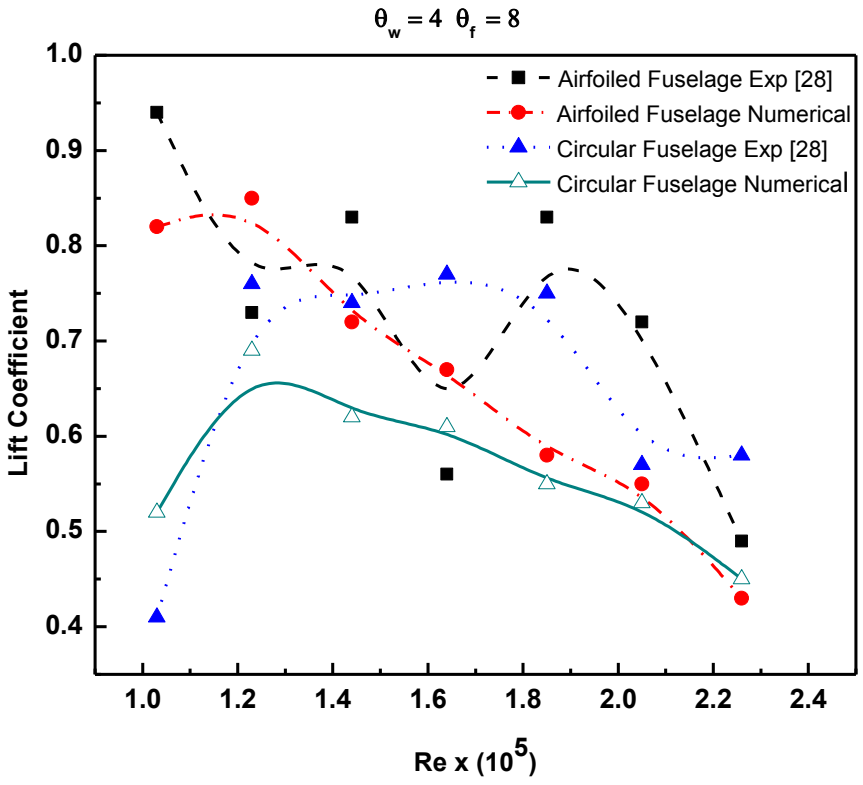

Fig. 5.11(a) Lift coefficient vs. Reynolds number curve for θ_w=4^o, θ_f = 8^o

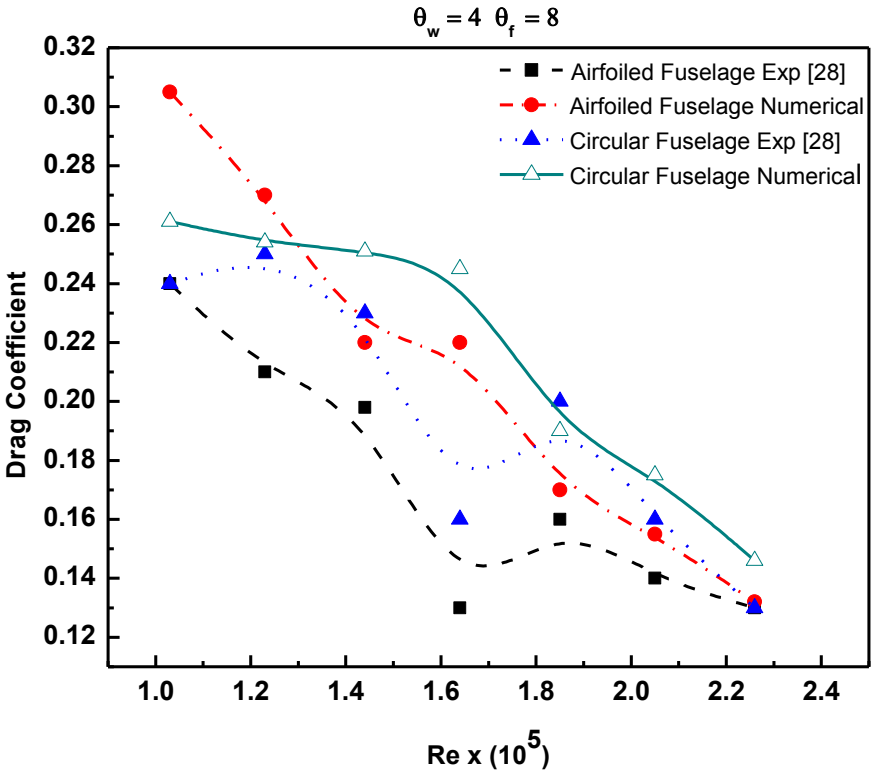

Fig. 5.11(b) Drag coefficient vs. Reynolds number curve for θ_w=4^o, θ_f =

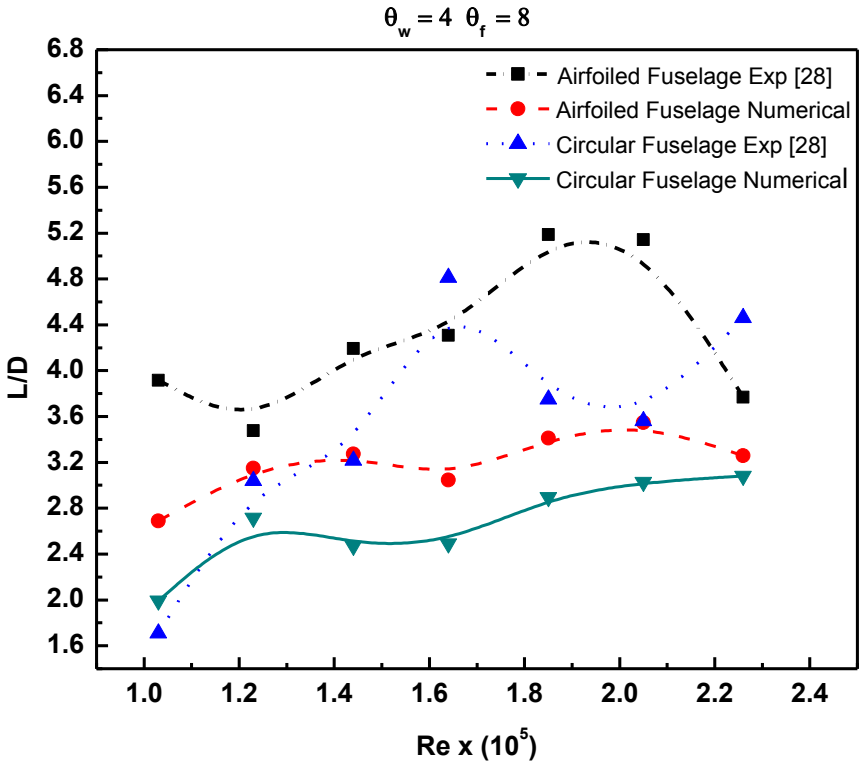

8^o

Fig. 5.11(c) L/D vs. Reynolds number curve for θ_w=4^o, θ_f = 8^o

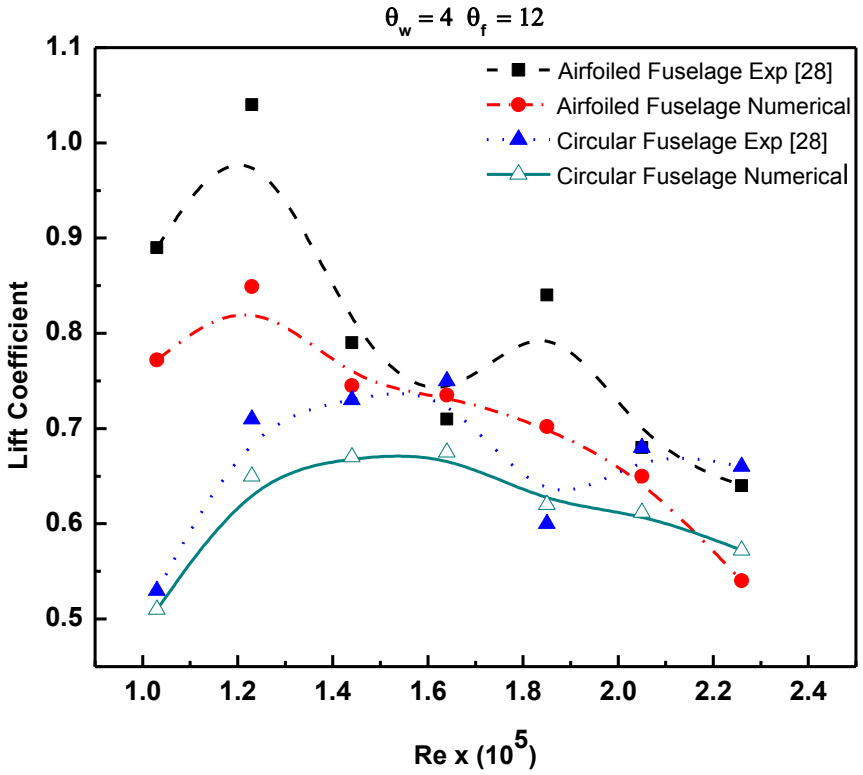

Fig. 5.12(a) Lift coefficient vs. Reynolds number curve for θ_w=4^o, θ_f = 12^o

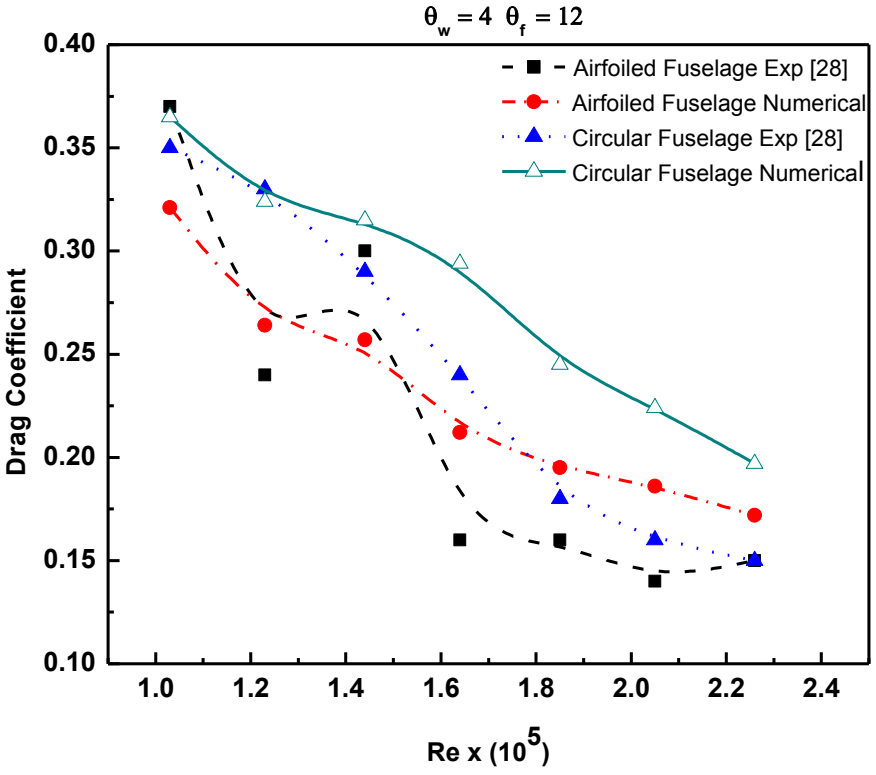

Fig. 5.12(b) Drag coefficient vs. Reynolds number curve for θ_w=4^o, θ_f = 12^o

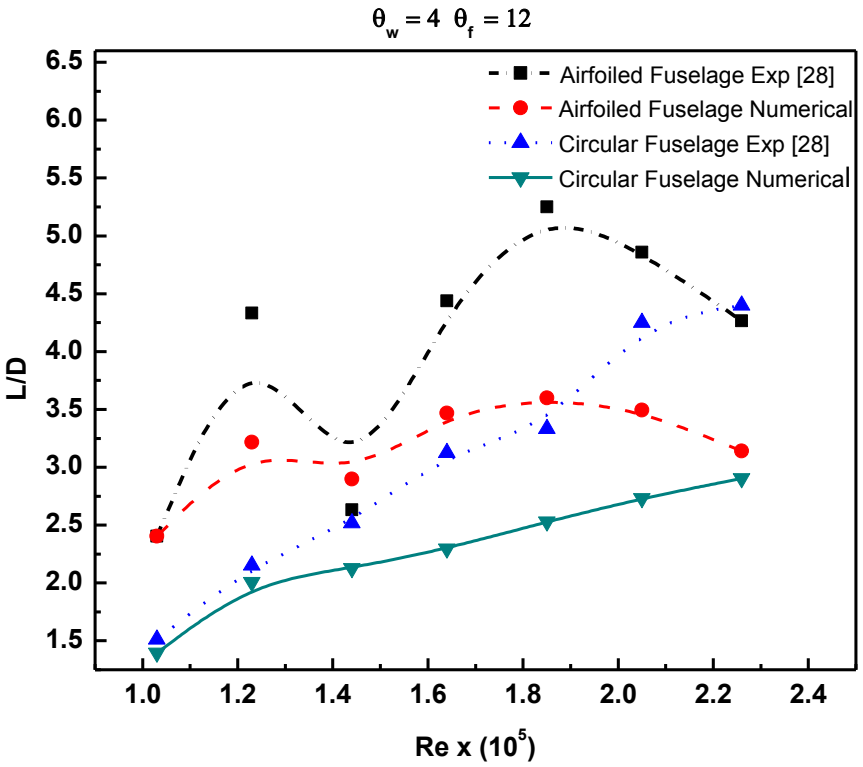

Fig. 5.12(c) L/D vs. Reynolds number curve for θ_w=4^o, θ_f = 12^o

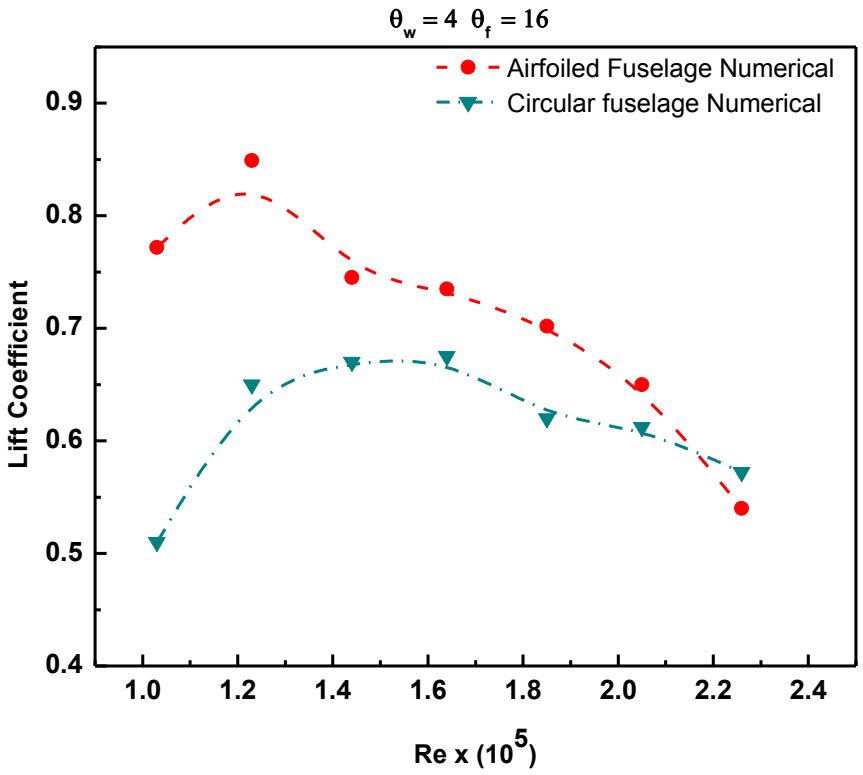

Fig. 5.13(a) Lift coefficient vs. Reynolds number curve for θ_w=4^o, θ_f = 16^o

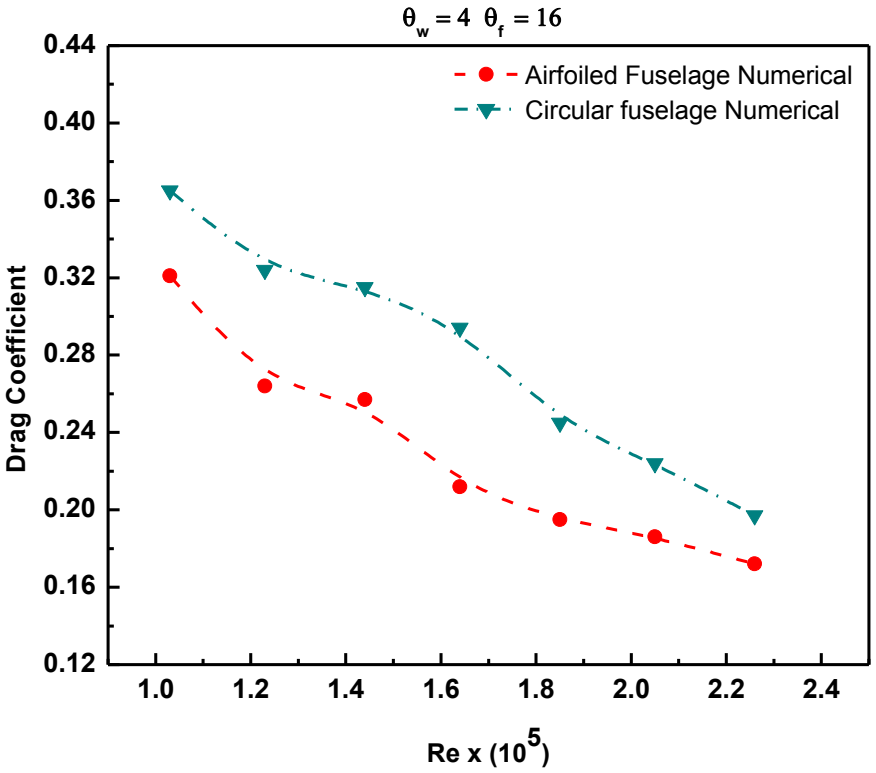

Fig. 5.13(b) Drag coefficient vs. Reynolds number curve for θ_w=4°, θ_f = 16°

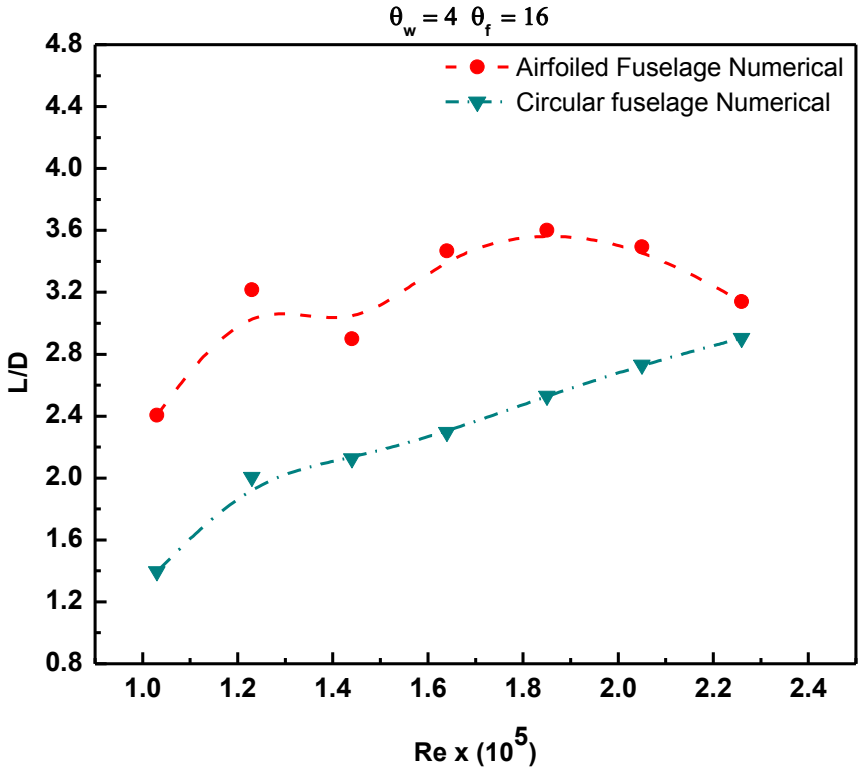

Fig. 5.13(c) L/D vs. Reynolds number curve for θ_w=4°, θ_f = 16°

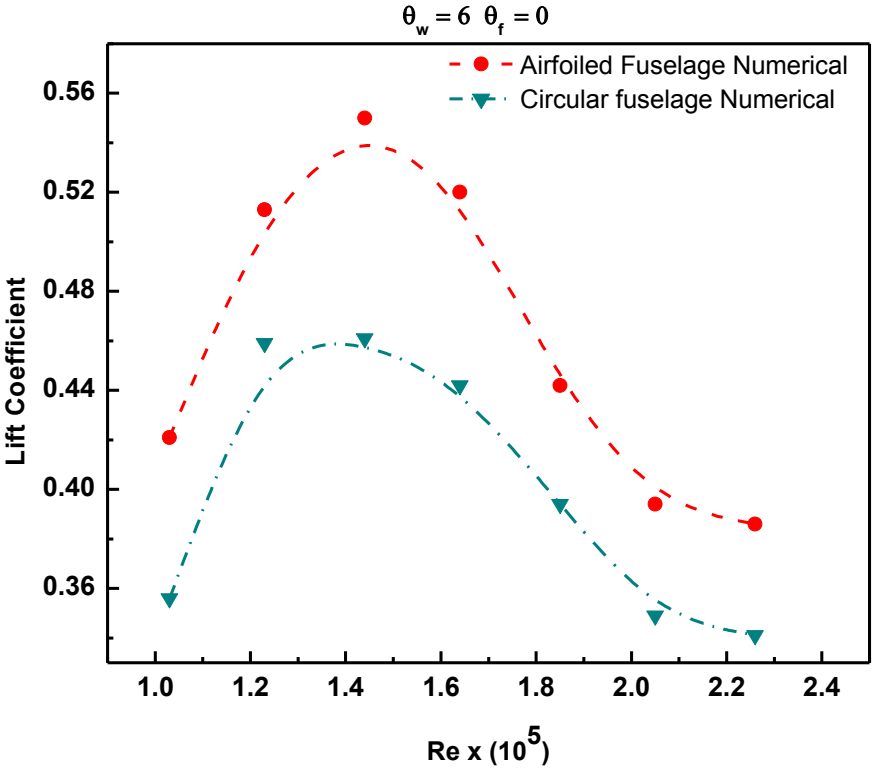

Fig. 5.14(a) Lift coefficient vs. Reynolds number curve for θ_w=6^o, θ_f =

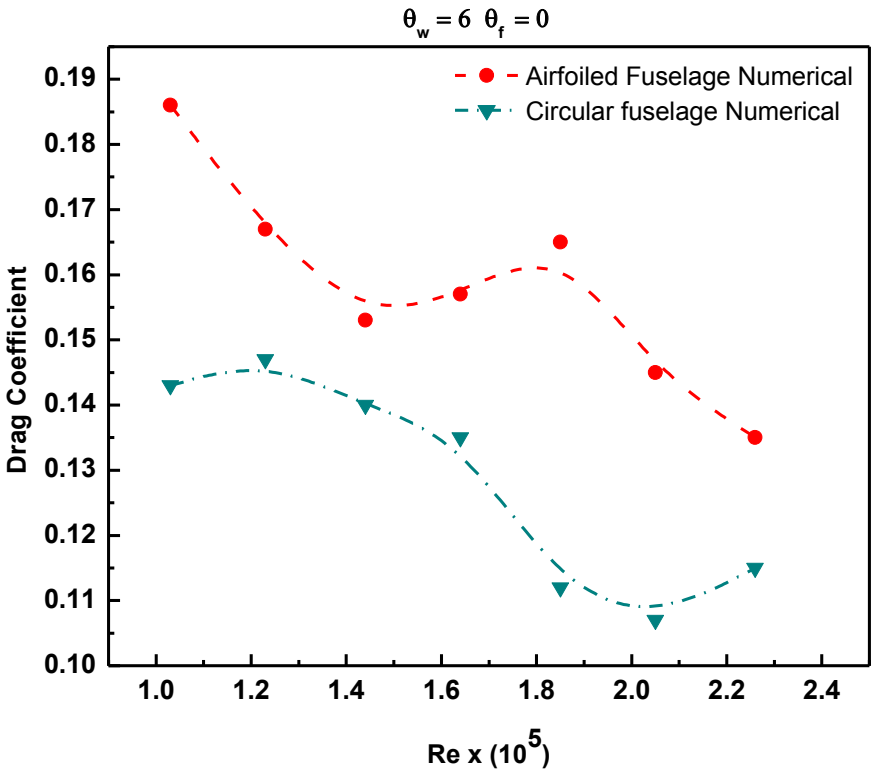

0^o

Fig. 5.14(b) Drag coefficient vs. Reynolds number curve for θ_w=6^o, θ_f = 0^o

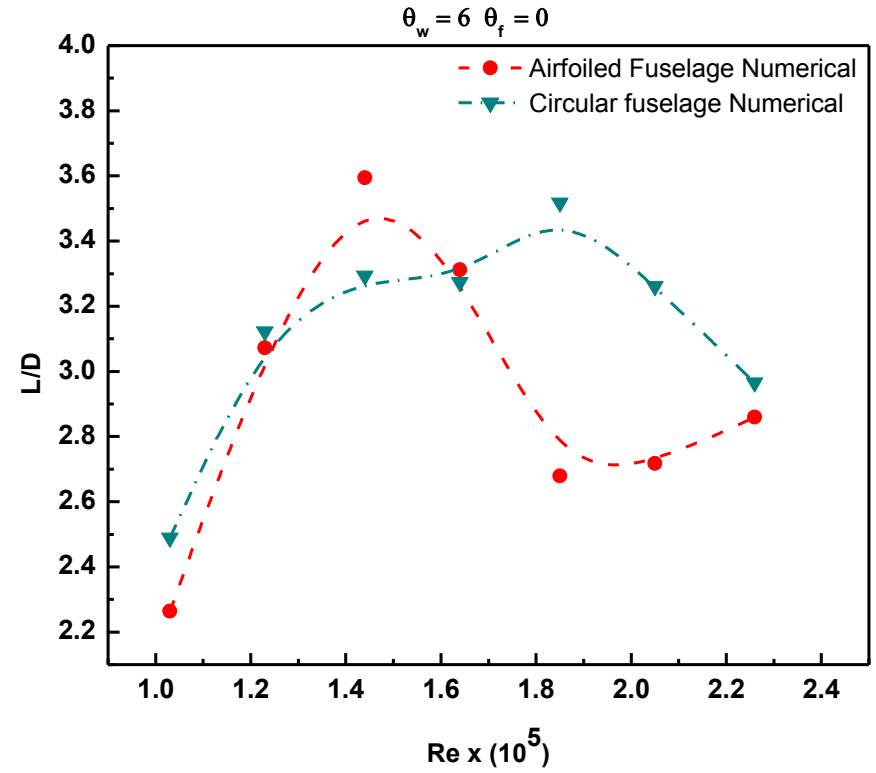

Fig. 5.14(c) L/D vs. Reynolds number curve for θ_w=6^o, θ_f = 0^o

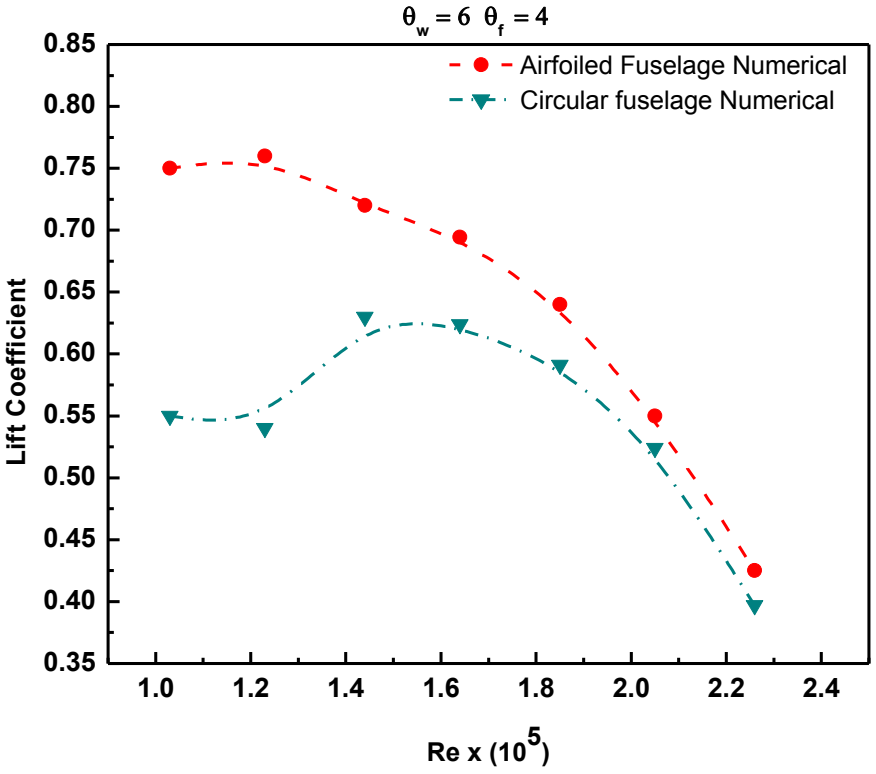

Fig. 5.15(a) Lift Coefficient vs. Reynolds number curve for θ_w=6^o, θ_f = 4^o

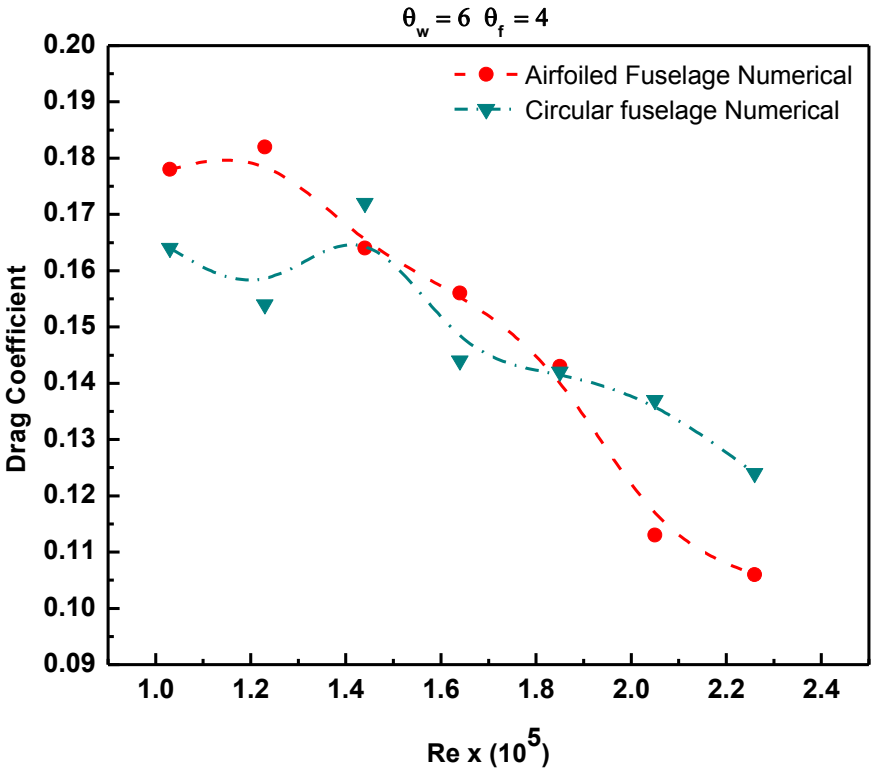

Fig. 5.15(b) Drag coefficient vs. Reynolds number curve for θ_w=6^o, θ_f =

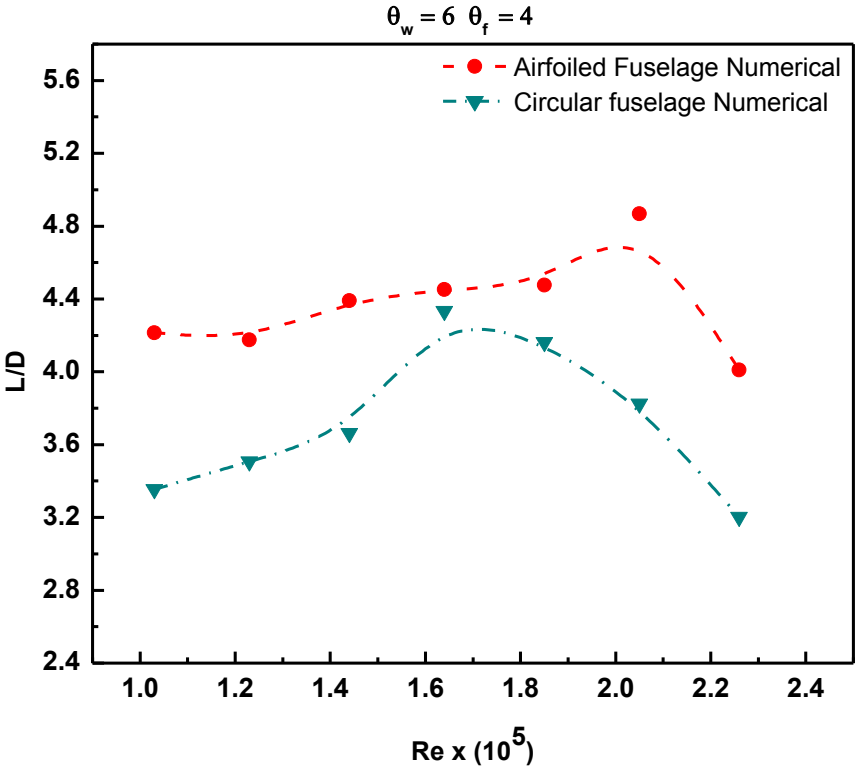

4^o

Fig. 5.15(c) L/D vs. Reynolds number curve for θ_w=6^o, θ_f = 4^o

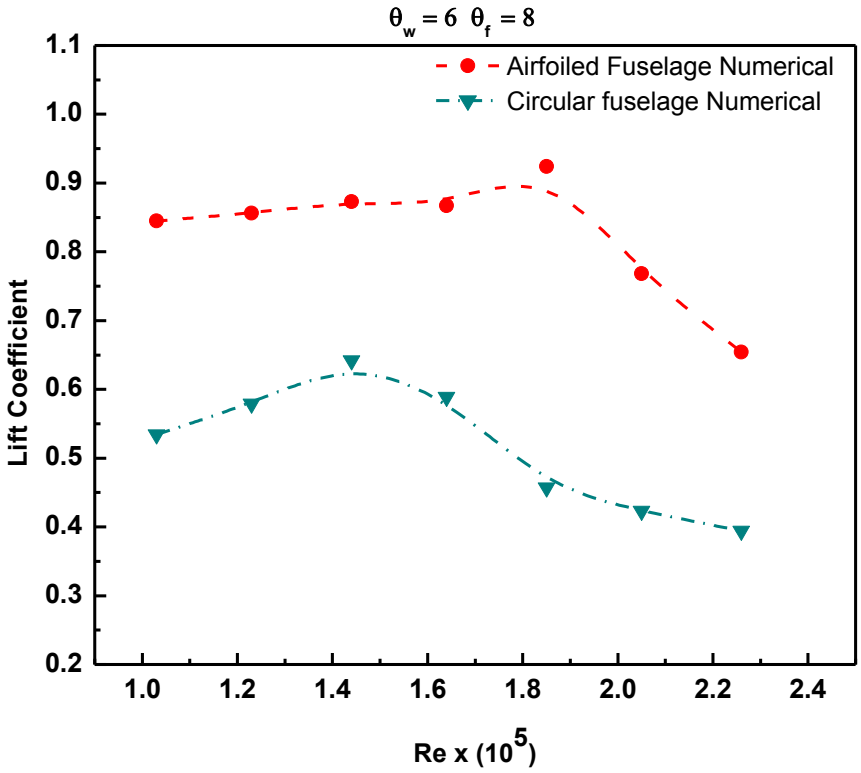

Fi

g. 5.16(a)Lift coefficient vs. Reynolds number curve for θ_w=6^o, θ_f =

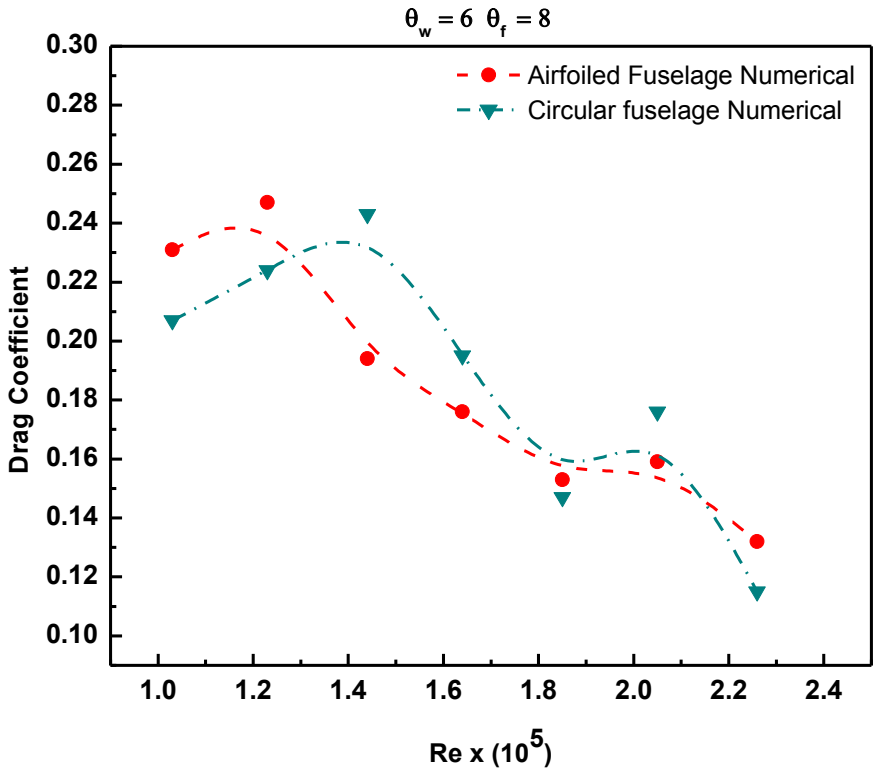

8^o

Fig. 5.16(b) Drag coefficient vs. Reynolds number curve for θ_w=6^o, θ_f = 8^o

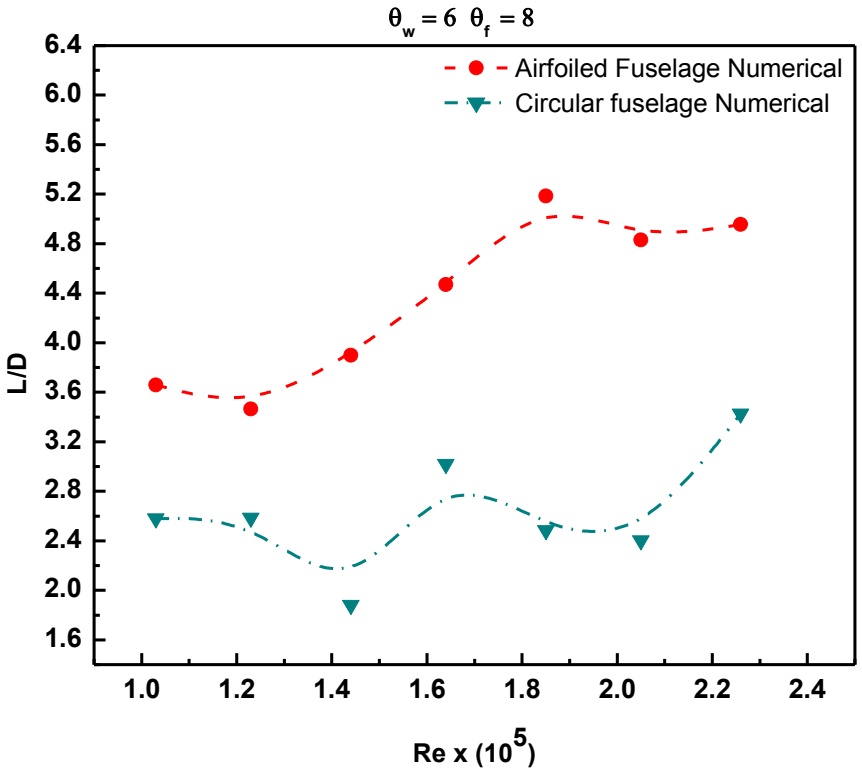

Fig. 5.16(c) L/D vs. Reynolds number curve for θ_w=6^o, θ_f = 8^o

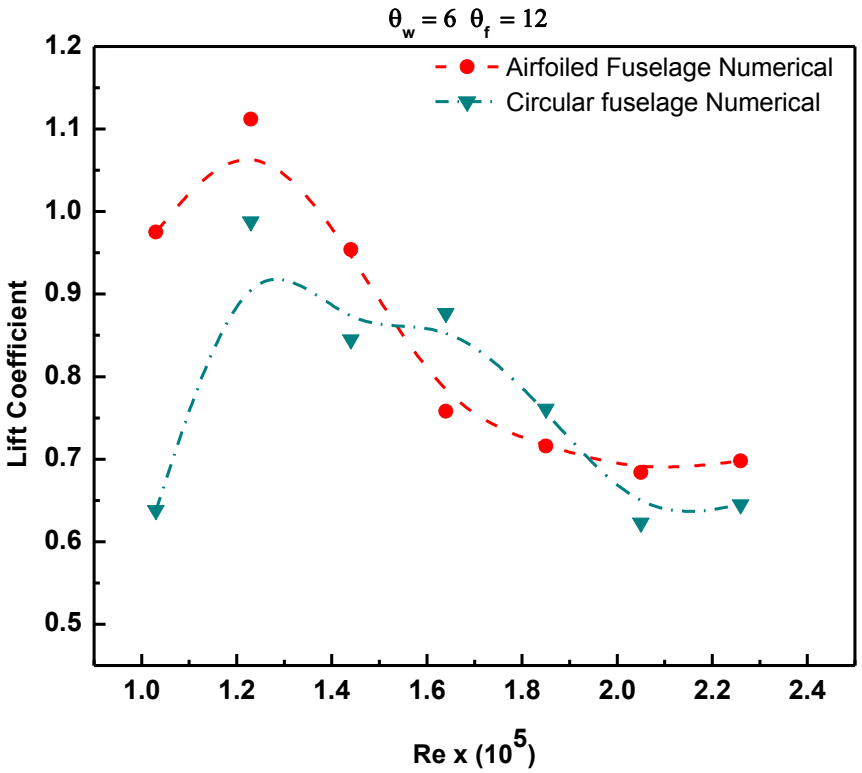

Fig. 5.17(a) Lift coefficient vs. Reynolds number curve for θ_w=6^o, θ_f = 12^o

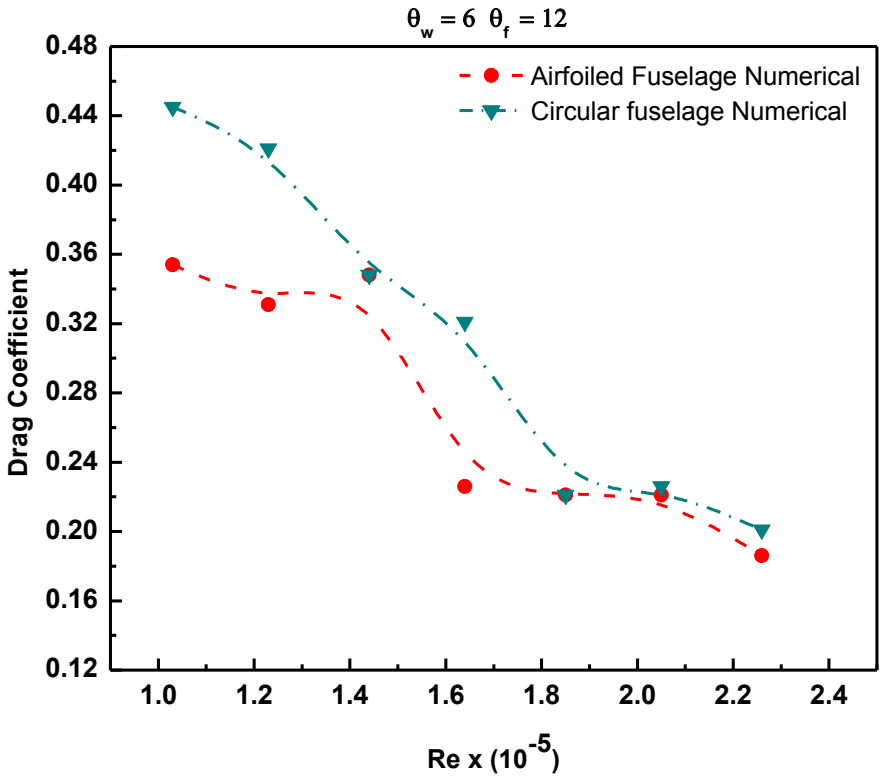

Fig. 5.17(b)Drag coefficient vs. Reynolds number curve for θ_w=6^o, θ_f = 12^o

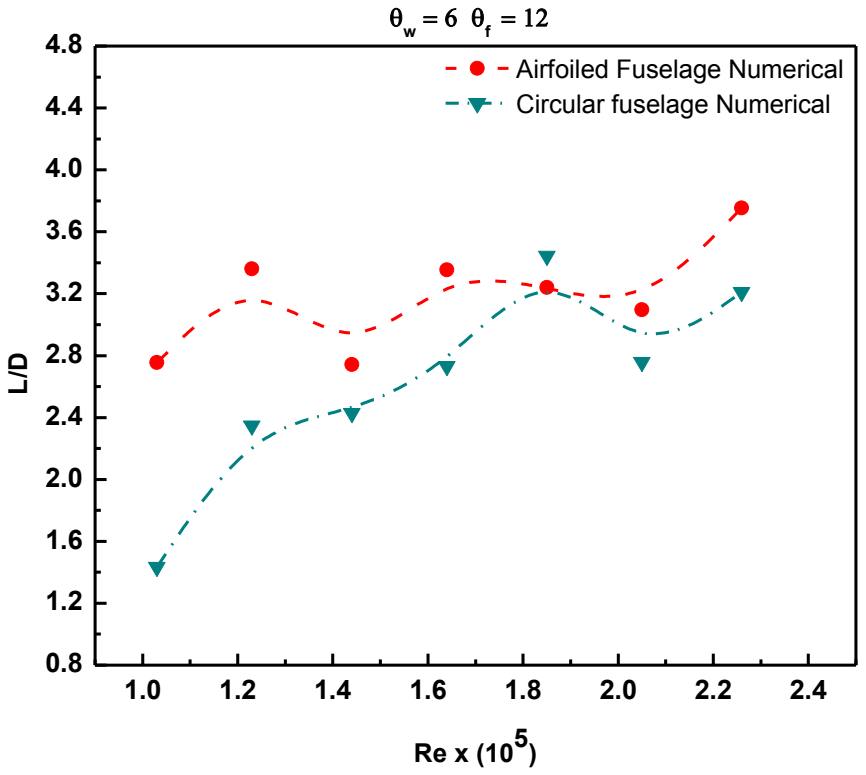

Fig. 5.17(c) L/D vs. Reynolds number curve for θ_w=6^o, θ_f = 12^o

CHAPTER 6
CONCLUSION AND RECOMMENDATION

6.1 Concluding Remarks

Some important conclusions that can be drawn from this thesis are briefly discussed below:

- From the analysis of lift to drag ratio curves it can be concluded that the minimum speed required to take off is decreased from circular fuselage model to airfoiled fuselage model.

- From the drag coefficient vs. Reynolds No. curves it is seen that the drag crisis is quite visible in the velocity range from 80 km/hr ($Re = 1.64\times10^5$) to 100 km/hr ($Re = 2.05\times10^5$) for the airfoiled fuselage model.

- During take-off, a higher angle of attack of the fuselage reduces the takeoff speed; thereby it will require a shorter runway and less takeoff time at operating condition.

- Although airfoiled fuselages provide a greater lift over circular fuselage but overall lift to drag ratio is reduced due to induced drag in airfoil fuselages.

- Lift to drag ratio of airfoiled fuselages is higher than circular fuselages at high angle of attack although at lower flow angle circular fuselages exhibit higher lift to drag ratio.

- Wing angle relative to fuselage $\theta_w = 6^o$ provides the maximum lift corresponding to a drag when this airplane fly with fuselage angle of attack, $\theta_f = 4^o$.

6.2 Recommendations for Future Work

Some recommendations for further work are as follows:

- In this thesis, at the finite width airfoiled fuselage, due to tip vortices induced drag is generated, which reduces the overall lift to drag ratio to a great extent, which can largely be reduced by incorporating winglets at both side of the

airfoiled fuselages. Addition of winglets at the wings will also improve the overall lift to drag ratio. So, in future work simulation can be conducted for airfoiled fuselages with winglets.

- This research work did not consider the moment forces on the models which have a greater influence on the stability of an airplane. So the whole investigation can be done by considering the moment forces on the models.

- This simulation is carried out in a very limited computational resource. Conducting this research in a workstation would give more flexibility to use more refined mesh, which subsequently would improve the results.

- The flow characteristics and pressure distribution around the airplane should be measured to know the behavior of flow separation, wake formation and circulation around it as these greatly influence its lift and drag characteristics.

- Blended Wing Body (BWB) concepts are frequently being considered in modern aircraft designs. In this research the birds body shapes are considered as airfoiled shapes but their body shapes are also an example of BWB. So a comparison between Circular fuselage, Airfoiled fuselage and Blended Wing Body fuselage will be more practical.

REFERENCES

[1] Levy, H. and Riding, R., "Burnelli's Lifting Fuselages." Aeroplane Monthly, Vol. 8, No.7, July 1980, pp. 348-350.

[2] Levy, H., "Burnelli Lifting Fuselage Projects." Aeroplane Monthly, Vol. 8, No. 10, Oct. 1980, pp.516-517. 6. Wood, R. M. and Bauer, S. X. S.: Flying Wings/Flying Fuselages. AIAA 2001-0311, Jan. 8-11, 2001.

[3] Cantilli, E., "Saga of the Lifting Body/Flying Wing." Flight, pp. 56-61, Fall 1996.

[4] Mitchell, K. A., "Burnelli and His Lifting-Body Transports." American Aviation Historical Society Journal, pp. 2-19, Spring 1997.

[5] Riding, R., "Burnelli's Lifting Fuselages." Aeroplane Monthly, Vol. 8, No. 6, June 1980, pp. 329-331.

[6] Wood R. M., "The Contributions of Vincent Justus Burnelli" AIAA 2003-0292, Jun. 2003.

[7] Wertenson, I. F., "Investigation of the Burnelli Type Airplane" Jan. 1931.

[8] Wertenson, I. F., "Investigation into the Development of the Burnelli Type Airplane" Aero Digest, March 1931.

[9] Wertenson, F., "The Economical Cruising Speed of the Burnelli All-Wing Monoplane Flight" Aug. 24, 1933, pp. 854-856.

[10] Klemin, A., "All-Wing Lifting Fuselage, Scientific America" April 1935.

[11] Burnelli Model UB-14 14-Passenger Transport Aero Digest, August 1935.

[12] Watter, M., "The Burnelli Airfoil Body. Flight" The Aircraft Engineer, Sept 26, 1935.

[13] Wood, R. M. and Bauer, S. X. S. "Flying Wings/Flying Fuselages" AIAA 2001-0311, Jan. 8-11, 2001.

[14] http://www1.msfc.nasa.gov/Newsroom/news/releases/2002/02-182.html, November 2002.

[15] Jenkins D. R., Landis T., and Miller J., "American X-Vehicles, An Inventory—X-1 to X-50, Centennial of Flight Edition, Monographs in Aerospace" History No. 31, SP-2003-4531, June 2003.

[16] Hansen J. R., Kinney J., "Taylor D. B., Prickett M., and Lee J. L., The Wind and Beyond, A Documentary Journey into the History of Aerodynamics in America" Volume II: Reinventing the Airplane June 2000.

[17] Tucker V. A., "Gliding Birds: Reduction of Induced Drag by Wing Tip Slots Between the Primary Feathers" Department of Zoology, Duke University, Durham, NC 27706, USA, 1993.

[18] Hummel, D. (1980), "The aerodynamic characteristics of slotted wing-tips in soaring birds." In Acta XVII Congressus Internationalis Ornithologici (ed. R. Nöhring), pp. 391–396.

[19] Munk, M. M. (1921), "The minimum induced drag of airfoils." National Advisory Committee for Aeronautics Tech. Rept121.

[20] Tucker, V. A. (1987), "Gliding birds: the effect of variable wing span." J. exp. Biol, 133, 33–58.

[21] Tucker, V. A. (1990), "Measuring aerodynamic interference drag between a bird body and the mounting strut of a drag balance." J. exp. Biol. 154, 439–461.

[22] Tucker, V. A. (1992), "Pitching equilibrium, wing span and tail span in a gliding Harris' hawk, *Parabuteo unicinctus*." J. exp. Biol. 165, 21–41.

[23] Tucker, V. A. and Heine, C. (1990), "Aerodynamics of gliding flight in a Harris' hawk, *Parabuteo unicinctus*." J. exp. Biol. 149, 469–489.

[24] Tucker, V. A. and Parrott, G. C. (1970), "Aerodynamics of gliding flight in a falcon and other birds." J. exp. Biol. 52, 345–367.

[25] Eastman N. Jacobs and Albert Sherman, “Wing-Fuselage interference comparison of conventional and aerofoil type fuselage combination.” March 1937.

[26] I. Kroo Stanford University, U.S.A. “Nonplanar wing concepts for increased aircraft efficiency” VKI lecture series on Innovative Configurations and Advanced Concepts for Future Civil Aircraft, June 6-10, 2005

[27] J. Reneaux, Onera, Applied Aerodynamics Department “Overview on drag reduction technologies for civil transport aircraft” *European Congress on Computational Methods in Applied Sciences and Engineering (ECCOMAS),* 2004.

[28] Mainuddin, M., *Experimental Investigation of Lift to Drag Ratio between Volumetrically Equivalent Fuselages*, M. Sc. Engg. Thesis, Department of Mechanical Engineering, Bangladesh University of Engineering and Technology, 2009.

[29] Douglas, J. F., Gasiorek J. M., and J. A. Swaffield, “Fluid Mechanics,” Pages 327-332, Longman publishers.

[30] Abbott, H. I., and Doenhoff, V., “Theory of Wing Sections” Dover publication Inc, Newyork, 1958.

[31] Silisteanu, and P. Botez, P.A., “Transition-flow-occurrence estimation; A new approach”, *Journal of Aircraft*, Vol. 47, No. 2

[32] Kermode, A.C, “Mechanics of Flight”, Pearson Education, 2006.